

# Multiscale modeling of large deformation in geomechanics

Weijian Liang | Jidong Zhao 

Department of Civil and Environmental Engineering, Hong Kong University of Science and Technology, Hong Kong

## Correspondence

Jidong Zhao, Department of Civil and Environmental Engineering, Hong Kong University of Science and Technology, Hong Kong.  
Email: jzhao@ust.hk

## Funding information

National Natural Science Foundation of China, Grant/Award Number: 51679207; Research Grants Council of Hong Kong, Grant/Award Number: T22-603/15-N; General Research Fund, Grant/Award Number: 16210017

## Summary

Large deformation soil behavior underpins the operation and performance for a wide range of key geotechnical structures and needs to be properly considered in their modeling, analysis, and design. The material point method (MPM) has gained increasing popularity recently over conventional numerical methods such as finite element method (FEM) in tackling large deformation problems. In this study, we present a novel hierarchical coupling scheme to integrate MPM with discrete element method (DEM) for multiscale modeling of large deformation in geomechanics. The MPM is employed to treat a typical boundary value problem that may experience large deformation, and the DEM is used to derive the nonlinear material response from small strain to finite strain required by MPM for each of its material points. The proposed coupling framework not only inherits the advantages of MPM in tackling large deformation engineering problems over the use of FEM (eg, no need for remeshing to avoid mesh distortion in FEM), but also helps avoid the need for complicated, phenomenological assumptions on constitutive material models for soil exhibiting high nonlinearity at finite strain. The proposed framework lends great convenience for us to relate rich grain-scale information and key micromechanical mechanisms to macroscopic observations of granular soils over all deformation levels, from initial small-strain stage en route to large deformation regime before failure. Several classic geomechanics examples are used to demonstrate the key features the new MPM/DEM framework can offer on large deformation simulations, including biaxial compression test, rigid footing, soil-pipe interaction, and soil column collapse.

## KEYWORDS

DEM, geomechanics, hierarchical coupling, large deformation, multiscale modeling, MPM

## 1 | INTRODUCTION

Large deformation in soils may significantly affect the operation and serviceability for a wide range of geotechnical structures and applications, including footing foundation on soft soils, slope creep and failure, pile penetration, and sea-bed pipeline installation and maintenance. Safe design and analysis of these structures need to properly consider soil behavior at large deformation. Numerical modeling of large deformation in soils has long been known challenging, mainly because of two major difficulties commonly encountered. (a) Large deformation may likely induce changes in boundary conditions and how soil interacts with the surrounding structures, and (b) the behavior of soil is highly nonlinear and is

loading history and state-dependent, especially at large deformation. To tackle both geometric nonlinearity and material nonlinearity has become the major concerns on large deformation modeling of soils.

Being one of the most successful numerical methods for the past half century, finite element method (FEM) has been widely used in all areas in geotechnical engineering. Conventional FEM based on updated Lagrangian formulation, however, cannot be readily applied for large deformation problems as it may suffer issues such as severe mesh distortion, inaccurate and inefficient computation, and possible nonconvergent solutions. Remedy measures such as remeshing or adaptive mesh<sup>1-7</sup> may help partially alleviate these issues, but cannot always guarantee convergence and may often cause considerable increase in computational cost.<sup>8</sup> The new millennium has witnessed the burgeoning of a variety of mesh-free methods with great potential to effectively address the large deformation problems. Representative ones include particle finite element methods (PFEM),<sup>9</sup> smooth particle hydrodynamics (SPH),<sup>10,11</sup> reproducing kernel particle method (RKPM),<sup>12,13</sup> and material point method (MPM).<sup>14-16</sup> These methods share a common feature to discretize a continuum domain by a set of points instead of elements. In doing so, the mesh distortion problem suffered by mesh-based methods such as FEM can be avoided. Among them, the MPM proposed 20 years ago<sup>14-16</sup> has enjoyed a particular popularity recently in geomechanics. Similar to general mesh-free methods, MPM discretizes a continuum body with a set of Lagrangian material points (or particles). Carrying essential information of the state parameters, these points are tracked throughout the computation of MPM. It departs from other mesh-free methods in that the MPM particles do not interact with one another directly, and the momentum equations are not solved on particles either. Rather, the momentum equations are resolved on a fixed Eulerian background mesh wherein the material particles are placed. As such, MPM presents a robust combination of Lagrangian (particles) and Eulerian (background mesh) descriptions, making it an ideal tool for modeling large deformation problems with complex boundaries. Moreover, MPM expedites the tracking of contacts in contact problems by allowing multiple velocity fields at mesh nodes. This is an amiable feature for modeling practical problems where contacts are important. MPM has been successfully applied in simulating a wide range of geotechnical problems, including foundation settlement,<sup>17</sup> pile installation,<sup>18,19</sup> column collapse,<sup>17,20,21</sup> silo discharge,<sup>22</sup> and landslide or landslide-induced flow.<sup>21,23,24</sup> More recently, MPM has also been extended to considering pore water pressure to simulate hydro-mechanical coupling problems. Examples reported in the literature include levee<sup>25-27</sup> and slope failures<sup>28</sup> (see a recent review on MPM by Soga *et al*<sup>27</sup>).

Same as any continuum approaches, MPM needs constitutive models to describe the mechanical response at its material particles. Granular soils are typical frictional materials showing high nonlinearity and history/loading path dependency. Continuum constitutive descriptions for the small-strain behavior of granular soils already prove to be laborious and complex, routinely requiring quite a few phenomenological model parameters that do not bear clear physical meanings. When more complicated material features such as strain localization,<sup>29</sup> anisotropy,<sup>30-32</sup> cyclic behavior, liquefaction, and critical state<sup>33-35</sup> have to be accounted for in a model, both the needed model parameters and the necessary model complexity quickly increase to such an extent that the model can hardly be comprehended by nonspecialists, let alone to be used by practising engineers. As mentioned before, the situation may be further grievously exacerbated in case of large deformation. Simple models applicable to small strain regimes may no longer be serviceable for large deformation conditions or regimes. Typically, a practical boundary value problem may involve a majority of its domain experiencing small strains, while only a small portion exhibiting large deformation (such as the footing problem to be treated in this paper). The discrete element method (DEM)<sup>36</sup> provides a paradigm-shifting weapon for constitutive modelers to investigate soil behaviors through all deformation regimes and under variable loading conditions, without having to resort to complex phenomenological assumptions. On the basis of relatively simple granular physics for an assembly of particles, DEM can faithfully reproduce the complex mechanical behavior of granular materials observed in laboratory tests. It may also offer rich microscopic information, such as the evolution of fabric anisotropy and force chain network.<sup>37</sup> The particle-scale information derived from DEM is widely conceived inspirational and insightful for constitutive modelers to understand perplexing macroscopic phenomena in granular materials, which otherwise are hard to attain through phenomenological models. Notwithstanding the benefit it may bring forth, DEM in its current stage remains unrealistic to provide any meaningful predictions for an engineering-scale problem. Its predictive capabilities are largely limited by the total number of particles it can model and the needed computational cost, the extent how natural sand grain morphology and surface characteristics are approximated and how reliable the grain-scale parameters are determined. As a view well shared by many, DEM remains at the moment a small-scale simulation tool (or “virtual sand box”), with a potential to replace many routine element tests in soil lab.<sup>37-41</sup>

A recent campaign, initiated by both DEM users and constitutive modelers, has been to push a marriage between continuum approaches with discrete methods to establish a hierarchically or concurrently coupled framework for geotechnical

modeling. Among many attempts, the hierarchical multiscale approach based on coupled FEM/DEM<sup>42-44</sup> has drawn particular attentions. This approach takes advantage of the predictive power of FEM in handling complex boundary value problems and the capacity of DEM in reproducing nonlinear material response of granular soils. It embeds a representative volume element (RVE) consisting of an assembly of discrete particles at each of the FEM Gauss integration points, passes the macro deformation information to the RVE as boundary conditions, and exploits the DEM to derive a solution for homogenized material responses (ie, stress and stiffness) to feed the macro FEM computation. The strategic marriage creates a win-win situation for both FEM and DEM. FEM no longer needs the assumption of complex phenomenological constitutive models, while DEM may now be connected to solving engineering-scale problems without being bothered by the excessive particle number and associated computational cost. Hierarchical FEM/DEM coupling has gained certain success in geomechanics applications, including the prediction of strain localizations in various boundary conditions,<sup>45-50</sup> geotechnical failures in footing and retaining walls,<sup>50</sup> and more recently, the compaction bands in sandstone.<sup>51</sup> However, the coupled FEM/DEM approach is not without pitfalls. Though it may somehow handle problems with relatively large rotation with consideration of the DEM part (see discussion in a study by Guo<sup>43</sup>), FEM cannot escape its doom on mesh distortion when the coupled approach is used to tackle large deformation problems. With all its merits, MPM stands out to be a good candidate to replace FEM in tackling such challenges.

We herein propose a new multiscale modeling approach based on hierarchical coupling of MPM and DEM, conceptually following a similar methodology outlined by Guo and Zhao,<sup>43,48</sup> to address large deformation in geomechanics. While tentative attempts have been made<sup>52-54</sup> along this line of research, the present one furnishes a first complete study on hierarchical coupling of MPM with DEM, providing detailed, innovative formulation, benchmarking, and demonstrative examples. We will demonstrate that the MPM and DEM are a perfect match to work together to capture both geometric and material nonlinearities arising in large deformation problems in a geotechnical setting. This approach has the potential to push a big step forward our cross-scale understanding of large deformation behavior pertaining to geotechnical failures.

This paper is organized as follows: Section 2 presents minimal essential formulations of MPM and DEM, with a detailed description on hierarchical coupling between them and the solution procedure. Benchmarking and demonstrative geomechanics examples, including biaxial shear tests, footing, pipe settling in sea-bed soil and soil column collapse, are given in Section 3, with detailed cross-scale analyses and discussion. We then conclude the paper with some major conclusions and future outlooks.

## 2 | HIERARCHICAL COUPLING OF MPM AND DEM: FORMULATION AND METHODOLOGY

### 2.1 | Material point method (MPM)

MPM was originally proposed by Sulusky and co-workers,<sup>14,15</sup> and was further generalized by Bardenhagen and Kober.<sup>16</sup> Similar to many other mesh-free methods, the continuum domain is discretized in MPM by a set of material points, each associated with essential state variables such as mass, velocity, strain, and stress. These material points move in a Lagrangian frame, and their movement represents the motion and deformation of the continuum body. Diverging from other mesh-free methods, MPM uses a background mesh to provide a Eulerian frame for calculation of spatial gradients and solving the discretized momentum equation. At each time step, the state variables are firstly mapped from the material points to the background grid nodes to establish the momentum equations. After the momentum equation is solved at the background mesh, the nodal solutions are mapped back to material points to update their velocities and positions. As the background mesh is fixed and does not move with the material points, MPM can avoid the issue of mesh distortion or entanglement and therefore handle large deformation effectively.

#### 2.1.1 | Governing equations and domain discretization

In MPM, the continuum body is represented by a set of material points with lumped mass. As the mass carried by each material point is assumed unchanged throughout the computation, the conservation of mass is implicitly satisfied. The motion and deformation are assumed to be governed by the momentum equations, and its weak form can be written as<sup>16,17</sup>:

$$\int_{\Omega} \rho \mathbf{a} \cdot \delta \mathbf{v} dx + \int_{\Omega} \boldsymbol{\sigma} : \nabla \delta \mathbf{v} dx = \int_{\Omega} \rho \mathbf{b} \cdot \delta \mathbf{v} dx + \int_{\partial\Omega} \boldsymbol{\tau} \cdot \delta \mathbf{v} dS, \quad (1)$$

where “.” denotes first-order vector contraction, “:” represents second-order tensor contraction, “ $\nabla$ ” denotes the gradient operator,  $\rho$  is current mass density,  $\mathbf{a}$  is the acceleration,  $\delta\mathbf{v}$  is an admissible velocity field,  $\boldsymbol{\sigma}$  is the Cauchy stress,  $\mathbf{b}$  is the body force,  $\boldsymbol{\tau}$  is the boundary traction, and  $\Omega$  and  $\partial\Omega$  represent the entire current domain of continuum and its boundary, respectively.

The continuum domain is first discretized into a set of material points defined by the characteristic function  $\chi_p(\mathbf{x})$ . This function represents the volume fraction of material point  $p$  at position  $\mathbf{x}$  of the macro scale domain and it satisfies the partition of unity in the initial configuration,<sup>16</sup> ie,

$$\sum_p \chi_p^i(\mathbf{x}) = 1 \quad \forall \mathbf{x}, \quad (2)$$

where the superscript  $i$  indicates the initial state. With the characteristic functions  $\chi_p(\mathbf{x})$ , each material point can be assigned its relevant state properties, including initial volume  $V_p^i$ , mass  $m_p^i$ , momentum  $\mathbf{p}_p^i$ , and Cauchy stress  $\boldsymbol{\sigma}_p^i$  according to:

$$V_p^i = \int_{\Omega^i} \chi_p^i(\mathbf{x}) d\mathbf{x}, \quad (3)$$

$$m_p^i = \int_{\Omega^i} \rho^i(\mathbf{x}) \chi_p^i(\mathbf{x}) d\mathbf{x}, \quad (4)$$

$$\mathbf{p}_p^i = \int_{\Omega^i} \rho^i(\mathbf{x}) \mathbf{v}^i(\mathbf{x}) \chi_p^i(\mathbf{x}) d\mathbf{x}, \quad (5)$$

$$\boldsymbol{\sigma}_p^i = \int_{\Omega^i} \frac{\boldsymbol{\sigma}^i(\mathbf{x})}{V_p^i} \chi_p^i(\mathbf{x}) d\mathbf{x}, \quad (6)$$

where  $\Omega^i$  is the initial domain of the continuum to be discretized,  $\rho^i(\mathbf{x})$  denotes initial mass density of the continuum, and  $\mathbf{v}^i(\mathbf{x})$  and  $\boldsymbol{\sigma}^i(\mathbf{x})$  are the initial velocity field and stress field, respectively.

After the initial discretization, any property  $f(\mathbf{x})$  of the continuum body can be expanded on a material point basis:

$$f(\mathbf{x}) = \sum_p f_p \chi_p(\mathbf{x}), \quad (7)$$

where  $f_p$  represents a material point property. Substituting Equation 7 into 1, the weak formulation of momentum conservation can be rewritten in the form of summation over material points:

$$\sum_p \int_{\Omega_p \cap \Omega} \frac{\dot{\mathbf{p}}_p}{V_p} \chi_p \cdot \delta\mathbf{v} d\mathbf{x} + \sum_p \int_{\Omega_p \cap \Omega} \boldsymbol{\sigma}_p \chi_p : \nabla \delta\mathbf{v} d\mathbf{x} = \sum_p \int_{\Omega_p \cap \Omega} \frac{m_p}{V_p} \chi_p \mathbf{b} \cdot \delta\mathbf{v} d\mathbf{x} + \int_{\partial\Omega} \boldsymbol{\tau} \cdot \delta\mathbf{v} dS, \quad (8)$$

where  $\Omega_p$  is current support of the characteristic function  $\chi_p$ , and  $\dot{\mathbf{p}}_p$  is the material time derivative of the material point momentum.

Because of the presence of the background mesh, the admissible velocity field  $\delta\mathbf{v}$  can be expanded in terms of the grid-based shape function by

$$\delta\mathbf{v} = \sum_I \delta\mathbf{v}_I N_I(\mathbf{x}), \quad (9)$$

where  $\delta\mathbf{v}_I$  is the value of admissible velocity taken at the node  $I$  and  $N_I(\mathbf{x})$  is the standard finite element shape function. Substituting Equation 9 into 8 and considering the arbitrariness of the admissible velocity field, the discrete momentum conservation is revised as:

$$\dot{\mathbf{p}}_I = \mathbf{f}_I^{int} + \mathbf{f}_I^{ext}, \quad (10)$$

where:

$$\dot{\mathbf{p}}_I = \sum_p \dot{\mathbf{p}}_p S_{Ip}, \quad (11)$$

$$\mathbf{f}_I^{int} = - \sum_p \boldsymbol{\sigma}_p \cdot \nabla S_{Ip} V_p, \quad (12)$$

$$\mathbf{f}_I^{ext} = \sum_p m_p \mathbf{b} S_{Ip} + \int_{\partial\Omega} N_I \boldsymbol{\tau} dS, \quad (13)$$

and,  $S_{Ip}$  is the weighting function, whereas  $\nabla S_{Ip}$  is the gradient weighting function:

$$S_{Ip} = \frac{1}{V_p} \int_{\Omega_p \cap \Omega} \chi_p(\mathbf{x}) N_I(\mathbf{x}) d\mathbf{x}, \quad (14)$$

$$\nabla S_{Ip} = \frac{1}{V_p} \int_{\Omega_p \cap \Omega} \chi_p(\mathbf{x}) \nabla N_I(\mathbf{x}) d\mathbf{x}. \quad (15)$$

As can be seen in Equations 10 to 15, the momentum equation is solved on the background mesh, which serves as a scratch pad for computing. Once the total force acting on the nodes of background mesh is computed, the momentum increment at each node can be obtained explicitly and further used to update the properties of material points, such as position and velocity. The update scheme and the complete computational procedure will be detailed in Section 2.1.2 and 2.3, respectively.

## 2.1.2 | Velocity update schemes: FLIP versus PIC

At the end of each calculation step, the updated nodal information is transferred back to the material points to update their positions and velocities. The material point positions  $\mathbf{x}_p$  are updated using the nodal velocity so that the numerical diffusion can be reduced<sup>55</sup>

$$\mathbf{x}_p^{n+1} = \mathbf{x}_p^n + \Delta t \sum_I \mathbf{v}_I^{n+1} S_{Ip}, \quad (16)$$

where  $\mathbf{v}_I^{n+1}$  is the updated velocity at node  $I$ ,  $\Delta t$  is the time step, and  $S_{Ip}$  is the weighting function mentioned in Equation 14.

Pertaining to velocity update, there are two conventional update schemes, ie, **P**article **I**n **C**ell (PIC)<sup>56</sup> and **F**Luid **I**mplicit **P**article (FLIP),<sup>57</sup> with the following expressions, respectively:

$$\mathbf{v}_{p,PIC}^{n+1} = \sum_I \mathbf{v}_I^{n+1} S_{Ip}, \quad (17)$$

$$\mathbf{v}_{p,FLIP}^{n+1} = \mathbf{v}_p^n + \Delta t \sum_I \mathbf{a}_I^{n+1} S_{Ip}, \quad (18)$$

where  $\mathbf{v}_{p,PIC}^{n+1}$  and  $\mathbf{v}_{p,FLIP}^{n+1}$  are the updated particle velocities based on PIC and FLIP, respectively.  $\mathbf{v}_p^n$  represents the material point velocity at the previous step and  $\mathbf{a}_I^{n+1}$  is the acceleration at node  $I$ . PIC directly uses the velocity extrapolated from nodes to overwrite current velocity. It can filter the velocities and helps the global computation to be more stable.<sup>58</sup> However, it may also suffer the issue of excessive energy dissipation, which is unacceptable for modelling dynamic problems (such as column collapse to be discussed later). In contrast, FLIP updates the material point velocity by a velocity increment computed from nodal acceleration. The issue of excessive energy dissipation can be avoided in FLIP at a cost of introducing some noise and reduced stability.<sup>58</sup>

For quasi-static problems, a proper combination of these two velocity update schemes may significantly improve the performance of MPM simulations,<sup>59,60</sup> such as a linear combination:

$$\mathbf{v}_p^{n+1} = \alpha_{PIC} \mathbf{v}_{p,PIC}^{n+1} + (1 - \alpha_{PIC}) \mathbf{v}_{p,FLIP}^{n+1}, \quad (19)$$

where  $\mathbf{v}_p^{n+1}$  denotes the updated particle velocity based on a linear combination of PIC and FLIP,  $\alpha_{PIC}$  is the PIC fraction in the particle velocity update:  $\alpha_{PIC} = 1$  represents the purely PIC velocity update, whilst  $\alpha_{PIC} = 0$  implies the FLIP velocity update. This fraction can be also interpreted as a kind of artificial damping to damp out any nonphysical or numerical oscillations.<sup>59</sup> In this study, a linear combination of PIC and FLIP with  $\alpha_{PIC} = 0.1$  is adopted for the velocity update in all the following numerical examples unless otherwise stated. This adopted PIC fraction value is consistent with that in Nairn and Stomakhin et al.,<sup>59,60</sup> which show a great improvement in simulations with this value. More advanced velocity update schemes, such as XPIC<sup>58</sup> and APIC,<sup>61</sup> can also be applied in proposed multiscale approach to achieve better performance. For simplicity, they are not considered in the present study.

## 2.2 | Discrete element method (DEM)

### 2.2.1 | Contact model

In a standard DEM, it is essential to determine the resultant acting on each particle via a contact model. Once a contact between two particles is established, the contact forces (normal contact force  $\mathbf{f}_n^c$  and tangential contact force  $\mathbf{f}_t^c$ ) can be calculated according to:

$$\mathbf{f}_n^c = -k_n^c \delta \mathbf{n} \quad (20)$$

$$\mathbf{f}_t^c = -\min(k_t^c u_t, |\mathbf{f}_n^c \tan \varphi|) \mathbf{t}, \quad (21)$$

where  $\mathbf{n}$  is the unit normal vector of the contact (see Figure 1),  $\mathbf{t}$  is the unit tangential vector,  $\delta$  is the overlap between two particles in contact,  $u_t$  is the relative tangential displacement,  $\varphi$  is the interparticle friction angle controlling the maximum magnitude of tangential contact force, and  $k_n^c$  and  $k_t^c$  are the normal contact stiffness and tangential (shear) contact stiffness, respectively. Two contact models, linear force-displacement contact model and nonlinear Hertz-Mindlin contact model,<sup>62</sup> are commonly used to determine the contact stiffnesses. The former considers contact stiffnesses ( $k_n^c$  and  $k_t^c$ ) as constants, whereas the nonlinear Hertz-Mindlin model assumes these two parameters vary with the contact overlap. In the paper, the linear force-displacement contact model is adopted:

$$k_n^c = \frac{2(E_i r_i)(E_j r_j)}{E_i r_i + E_j r_j}, \quad (22)$$

$$k_t^c = \frac{2(E_i r_i v_i)(E_j r_j v_j)}{E_i r_i v_i + E_j r_j v_j}, \quad (23)$$

where  $i$  and  $j$  denote the two particles in contact;  $E$ ,  $r$ , and  $v$  denote, respectively, the Young's modulus, the radius, and the Poisson's ratio of the contacting particle  $i$  or  $j$ .

Particle shape may be a pivotal feature for realistically reproducing the behavior of granular materials. Using idealized spheres/circular disks (3D/2D) in DEM simulation may potentially lead to the following discrepancies between the prediction and reality: (a) the macroscopic friction angle of a DEM packing may be found smaller than experimental result, (b) the energy loss because of rolling resistance is neglected in simulations, resulting in underestimated energy dissipation,<sup>63</sup> and (c) particle interlocking broadly existed in nature cannot be properly replicated by DEM simulations.

Though reproducing realistic particle shapes in DEM simulations may help to mitigate the above issues,<sup>64</sup> it is tremendously challenging to find a perfect solution for both rigorous morphological characterization and affordable computational efficiency. We hereby elect to choose a relatively simple and efficient alternative, by introducing rolling resistances between two contacting spheres/disks to partially remedy aforementioned issues. Similar to the tangential force, the resistant rolling moment,  $M_r^c$ , can be determined via:

$$M_r^c = -\min(|k_r^c \theta_r|, |\mathbf{f}_n^c r_{min} \eta|) \theta_r / |\theta_r|, \quad (24)$$

where  $\theta_r$  is the accumulated relative rotation angle between two contacting particles,  $r_{min} = \min(r_i, r_j)$  is the radius of the smaller particle,  $\eta$  is a dimensionless parameter defining the upper-bond limit of the resistant rolling moment, and  $k_r^c$  is the rolling stiffness which is related to the tangential contact stiffness  $k_t^c$ , though a dimensionless coefficient  $\beta$  for the contacting particle :

$$k_r^c = k_t^c r_i r_j \frac{2\beta_i \beta_j}{\beta_i + \beta_j}. \quad (25)$$

In case that two contacting particles are made of the same material (and thus have the same  $E$ ,  $v$ ,  $\beta$ , and  $\eta$ ), Equations 22, 23, and 25 can be simplified in terms of the harmonic mean of radii of the contacting particles,  $r^* = 2r_i r_j / (r_i + r_j)$ :

$$k_n^c = E r^*, \quad (26)$$

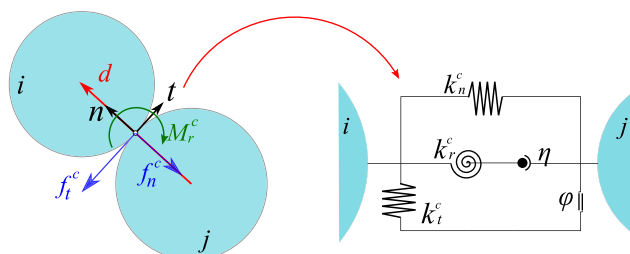


**FIGURE 1** Schematic of interparticle contact and contact model used in the discrete element method (DEM). A linear contact model with Coulomb's friction for normal and tangential contact directions in conjunction with a rolling resistance model on the contact moment is considered [Colour figure can be viewed at [wileyonlinelibrary.com](http://wileyonlinelibrary.com)]

$$k_t^c = E v r^*, \quad (27)$$

$$k_r^c = k_t^c r_i r_j \beta. \quad (28)$$

To dissipate undesired unbalance force  $\mathbf{f}_{unbal}$  and achieve quasi-static state in DEM, a numerical damping force  $\mathbf{f}_{damp}$  is applied to each particle :

$$\mathbf{f}_{damp} = -\alpha |\mathbf{f}_{unbal}| \mathbf{v}_p / |\mathbf{v}_p|, \quad (29)$$

where  $\alpha$  is the damping ratio, and  $\mathbf{v}_p$  is the velocity of the considered particle.

## 2.2.2 | Homogenization of material responses

### Stress tensor $\sigma$ , mean, and deviatoric stresses $p$ and $q$

A typical RVE in DEM is prepared by generating several number of disks (2D) or several thousand spheres (3D) in a cell with a periodic boundary, and is then consolidated to a desired initial state with specified pressure and void ratio.<sup>46,48</sup> It is then attached to each material point in the continuum MPM domain with prescribed deformation received from MPM solver as boundary conditions. Upon loading and reaching a quasi-static state in the DEM computation, a homogenized Cauchy stress  $\sigma$  can be extracted using the Love-Weber formula<sup>65,66</sup> and then passed to the MPM solver:

$$\sigma = \frac{1}{V} \sum_N \mathbf{d} \otimes \mathbf{f}^c, \quad (30)$$

where “ $\otimes$ ” denotes the dyadic product between two vectors,  $V$  is volume of the RVE,  $N$  is the total number of all contacts inside the RVE,  $\mathbf{d}$  is the branch vector joining the centers of contacting particles, and  $\mathbf{f}^c$  is the contact force.

On the basis of the average Cauchy stress, it is convenient to calculate two quantities commonly used in geomechanics, ie, the mean effective stress  $p$  and the deviatoric stress  $q$  (for 2D):

$$p = \frac{1}{2} \text{tr}(\sigma), \quad (31)$$

$$\mathbf{s} = \sigma - p \mathbf{I}, \quad (32)$$

$$q = \sqrt{\frac{1}{2} \mathbf{s} : \mathbf{s}}, \quad (33)$$

where “tr” indicates the trace of a tensor,  $\mathbf{s}$  is the deviatoric stress tensor, and  $\mathbf{I}$  is an identity tensor.

In addition, it is also instructive to derive the volumetric strain  $\epsilon_v$  and deviatoric strain  $\epsilon_q$ , the rotation angle  $\theta^*$ , and fabric anisotropy  $F_a$  for a RVE. These quantities could help to better understand the macroscopic behavior of the continuum.

### Volumetric and deviatoric strains $\epsilon_v$ and $\epsilon_q$

The volumetric and deviatoric strains,  $\epsilon_v$  and  $\epsilon_q$ , can be respectively computed according to:

$$\epsilon_v = \text{tr}(\epsilon), \quad (34)$$

$$\epsilon_q = \sqrt{2 \mathbf{e} : \mathbf{e}}, \quad (35)$$

where  $\epsilon$  is the strain tensor, and  $\mathbf{e} = \epsilon - \text{tr}(\epsilon) \mathbf{I}$  is the deviatoric strain tensor.

---

\*The rotation angle here refers to the cumulative rotation, which can be obtained via two means: one by directly calculating the cumulative rigid rotation of a MPM material point from the macro domain, and the other by extracting the average particle rotation of the RVE attached to the material point, as used in Guo and Zhao<sup>43</sup> and Wu et al<sup>51</sup> based on  $\theta_{avg} = \frac{1}{N_p} \sum_{p=1}^{N_p} \theta_p$  (where  $N_p$  is the number of particles in a RVE and  $\theta_p$  is the accumulated rotation angle of each particle). Our numerical experience indicates both rotation quantities offer similar trends and can be used as indicative variables for local analysis. For convenience, the first definition is adopted in the study in the following discussion.

### Rotation angle $\theta$

We consider the following decomposition of the deformation gradient  $\mathbf{F}$ :

$$\mathbf{F} = \mathbf{R} \cdot \mathbf{U}, \quad (36)$$

where  $\mathbf{U}$  denotes the right stretch tensor, which is symmetric and positive definite; and  $\mathbf{R}$  is the orthogonal rotation tensor, which can be related to the rotation angle  $\theta$  according to:

$$\mathbf{R} = \begin{bmatrix} \cos \theta & -\sin \theta \\ \sin \theta & \cos \theta \end{bmatrix}. \quad (37)$$

Considering the following relationship:

$$\mathbf{F}^T \cdot \mathbf{F} = (\mathbf{R} \cdot \mathbf{U})^T \cdot (\mathbf{R} \cdot \mathbf{U}) = \mathbf{U}^T \cdot \mathbf{R}^T \cdot \mathbf{R} \cdot \mathbf{U} = \mathbf{U}^T \cdot \mathbf{U} = \mathbf{U} \cdot \mathbf{U} \quad (38)$$

we can firstly determine  $\mathbf{U}$  and  $\mathbf{R}$  by the following equations, and then use Equation 37 to obtain the rotation angle  $\theta$ .

$$\mathbf{U} = (\mathbf{F}^T \cdot \mathbf{F})^{1/2} \quad (39)$$

$$\mathbf{R} = \mathbf{F} \cdot \mathbf{U}^{-1} \quad (40)$$

### Fabric anisotropy $\mathbf{F}_a$

Fabric anisotropy has been widely used to characterize the microstructure within an assembly of DEM particles during the loading process. In this study, we follow the contact-normal definition of fabric tensor proposed by Satake<sup>67</sup> and Oda<sup>68</sup> and determine the anisotropy intensity (for 2D):

$$\boldsymbol{\phi} = \frac{1}{N} \sum_N \mathbf{n} \otimes \mathbf{n} \quad (41)$$

$$\mathbf{F}_a = 4 \left( \boldsymbol{\phi} - \frac{1}{2} \mathbf{I} \right), \quad (42)$$

$$F_a = \sqrt{\frac{1}{2} \mathbf{F}_a : \mathbf{F}_a}, \quad (43)$$

where  $\boldsymbol{\phi}$  is the fabric tensor,  $\mathbf{F}_a$  is the deviatoric fabric tensor, and  $F_a$  is a scalar value used to measure anisotropy intensity.  $\mathbf{n}$  denotes the unit contact normal vector as shown in Figure 1.

## 2.3 | Hierarchical multiscale coupling between MPM and DEM

Figure 2 presents the flowchart of hierarchical multiscale coupling between MPM and DEM. A sequential interactive coupling scheme is followed. The macroscopic continuum domain is first discretized by MPM by a set of material points. Assemblies of granular particles with prescribed initial void ratio and confining pressure are generated and are assigned to the MPM material points as RVEs. Depending on the specific problem, identical or variable RVE assemblies can be assigned to the material points, leading to a homogeneous or inhomogeneous continuum domain. A typical coupling cycle comprises the following steps: (a) MPM is first employed to derive the motion and deformation for each material point under the prescribed boundary conditions. (b) The deformation information (typically the incremental displacement gradient  $d\mathbf{H}$ , consisting of the incremental strain  $\Delta\epsilon$ , and incremental rotation  $\Delta\omega$ ) at each material point is transferred to its corresponding RVE, serving as boundary conditions. (c) DEM is invoked to solve the RVE at the prescribed boundary conditions. (d) An updated Cauchy stress is homogenized over the deformed RVE configuration and is transferred back to its attached MPM material point for subsequent computation. Note that after each loading step, the deformed packing of each RVE is recorded as the initial state for the subsequent loading step. As such, the multiscale modeling may keep a memory of its past loading history over the whole domain. It is also noticed that the DEM computation for each RVE of the domain is independent, therefore it is straightforward to implement parallel computing to improve the computational efficiency of the multiscale modeling scheme.

Two open-source codes — *NairnMPM*<sup>69</sup> (MPM solver) and *YADE*<sup>70</sup> (DEM solver) have been rigorously coupled for implementation of the MPM/DEM multiscale approach. The following summarizes a complete solution procedure of the proposed scheme:

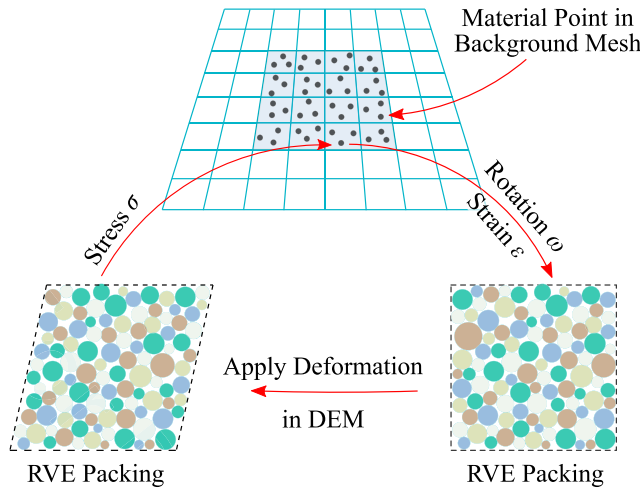


**FIGURE 2** Illustration of the hierarchical multiscale coupling scheme of material point method (MPM) and discrete element method (DEM) [Colour figure can be viewed at [wileyonlinelibrary.com](http://wileyonlinelibrary.com)]

Computation solution procedure for hierarchical coupling of MPM/DEM multiscale approach.

1. Discretize the continuum domain with material points and assign these points relevant quantities such as mass, volume, and initial stress using Equation 3 to 6. Attach an RVE with specified initial state to each material point.
2. Solution phase from step  $n$  to  $n + 1$ :
  - (a) Map from material points to nodes:
    - i. Compute nodal mass:  $m_I^n = \sum_p S_{Ip} m_p$ .
    - ii. Compute nodal momentum:  $p_I^n = \sum_p S_{Ip} p_p^n$ .
    - iii. Compute nodal velocity:  $v_I^n = p_I^n / m_I^n$ .
  - (b) Update deformation and stress of material points:
    - i. Compute material point incremental displacement gradient:  $d\mathbf{H}_p^{n+1} = \Delta t \sum_I \nabla S_{Ip} v_I^n$ .
    - ii. Update material point strain:  $\epsilon_p^{n+1} = \epsilon_p^n + \frac{1}{2} (d\mathbf{H}_p^{n+1} + (d\mathbf{H}_p^{n+1})^T)$ .
    - iii. Transfer  $d\mathbf{H}^{n+1}$  to corresponding RVE and apply deformation in DEM solver.
    - iv. Compute the homogenized Cauchy stress  $\sigma$  in DEM solver using Equation 30.
    - v. Transfer  $\sigma$  back to MPM and update particle stress:  $\sigma_p^{n+1} = \sigma$ .
  - (c) Solve momentum equation:
    - i. Compute internal force  $f_I^{int}$  and external force  $f_I^{ext}$  using Equations 12 and 13.
    - ii. Compute total nodal force:  $f_I = f_I^{int} + f_I^{ext}$ .
    - iii. Update nodal momentum:  $p_I^{n+1} = p_I^n + f_I \Delta t$ .
  - (d) Map from nodes to material points:
    - i. Update particle velocity using Equation 19.
    - ii. Update particle position using Equation 16.
3. Go to next step  $n + 1$ .

There are four noteworthy aspects about the coupled MPM/DEM multiscale approach:

- The MPM employs an explicit time integration scheme. The strain and stress at each material point are updated before the total nodal force is calculated, as this *update strain first* (USF) scheme has been argued to yield better *energy conservation* over the *update strain last* (USL) scheme.<sup>71</sup>
- Conventional continuum modeling of large deformation (and large rotation) needs the consideration of objective stress rate (eg, Jaumann stress rate) in constitutive formulations to ensure the objectiveness of the mechanical response. In the proposed MPM/DEM multiscale approach (see Step 2), an RVE receives the incremental displacement gradient  $d\mathbf{H}$  instead of pure strain increment  $\Delta\epsilon$  from the MPM, and thus the rotation is reflected in the RVE configuration. Moreover, the (total) updated stress  $\sigma$  is homogenized from the deformed RVE packing which may experience large rotation (as will be shown by examples in the next section), and hence, has implicitly incorporated the effect of rigid rotation. As such, the *objectiveness* of the local material response extracted from the RVE is retained in each step.
- In the current MPM/DEM coupling scheme, the only information that needs to be derived from a RVE is the Cauchy stress  $\sigma$  (not the stress increment), while in previous FEM/DEM approaches, the tangent operator is also needed in addition to stress.<sup>43</sup> Nevertheless, in possible future extension of the proposed MPM/DEM approach to hydro-mechanical coupling, more updated information may need to be extracted and passed on to the macro MPM computation, such as void ratio, fabric anisotropy, permeability (cf, Guo & Zhao<sup>72</sup>).
- Although a variety of remeshing or adaptive meshing techniques<sup>1,2,4-8,73,74</sup> have been proposed to enhance the capability of conventional FEM for tackling large deformation problems or strong discontinuity, they rarely work within the multiscale modeling framework for two reasons. The first and foremost important one is when applying these remeshing technique to multiscale modeling, we not only need to interpolate states variables (eg, stress, strain, and void ratio) from the old distorted mesh to the new one, but also have to map back the history of the microstructures (RVE history), and such attempt would ruin the physical basis for the multiscale framework. Secondly, a considerable number of specific RVE (whose stress states have to be compatible with local stress field) have to be generated and attached to additional Gauss interpolation points after each mesh refinement, this process is time-consuming and also substantially increases total elapse time for DEM solver (as more RVEs have to be solved). In contrast to FEM, the background mesh of MPM only serves as a “scratch pad” for solving the momentum equation, which will not distort during the computation, therefore there is no need for refinement or remapping, and the microstructures (RVE history) at a material point can be memorized throughout the simulation.

### 3 | MULTISCALE MODELING OF GEOMECHANICS PROBLEMS

In this section, the proposed hierarchical multiscale modeling approach based on coupled MPM and DEM is first benchmarked against single element test. It is then applied to predicting several classic geomechanics problems to showcase its predictive capability. The examples chosen here include strain localization in sand subjected to biaxial shear, failure of rigid footing foundation, soil-pipe interaction, and collapse of soil column. The biaxial shear example is also used to examine the sensitivity of multiscale predictions of strain localization to various model properties (eg, mesh sensitivity). Both the footing and the soil-pipe interaction problems feature multiscale predictions of quasi-static large deformation. The soil column collapse problem involves dynamic flow of soil to large deformation. Note that two-dimensional simulations are considered for all examples in this study for demonstration purposes, though the formulations (and implementation) have been developed based on full three-dimensional consideration.

#### 3.1 | Single element test

Single element test has been widely used for numerical model validations.<sup>43,49</sup> It is used here to benchmark the multiscale modeling approach. The single element is set up with prescribed boundary conditions as shown in Figure 3. A constant confining pressure ( $\sigma_{xx} = 100$  kPa) is applied to the right side of the element, and a vertical displacement is applied on the top surface. The left and bottom surfaces of the element are constrained by their horizontal and vertical degrees of freedom, respectively. An RVE with properties listed in Table 1 is generated and is isotropically consolidated to an initial mean stress  $p_0 = 100$  kPa and an initial void ratio  $e_0 = 0.177$  (which can be regarded as a dense packing). The single element domain is discretized by four material points in the MPM. An identical RVE is attached to each of the four points. Gravity is ignored in this simulation. As single element test is expected to generate homogeneous mechanical responses across the element, the global response measured from the element should match the local responses extracted from the pure DEM simulations under the same boundary conditions. Figure 4 depicts the global stress-strain relation

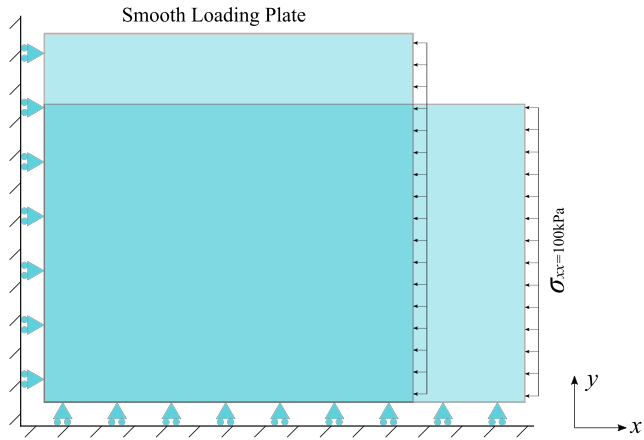


**FIGURE 3** Model setup for single element test [Colour figure can be viewed at wileyonlinelibrary.com]

**TABLE 1** Parameters for RVEs used in single element test

Particle Number	$r$ (mm)	$\rho$ (kg/m <sup>3</sup> )	$E$ (MPa)	$\nu$	$\varphi$ (°)	$\alpha$	$e_0$
400	3-7	2650	600	0.8	28.6	0.1	0.177

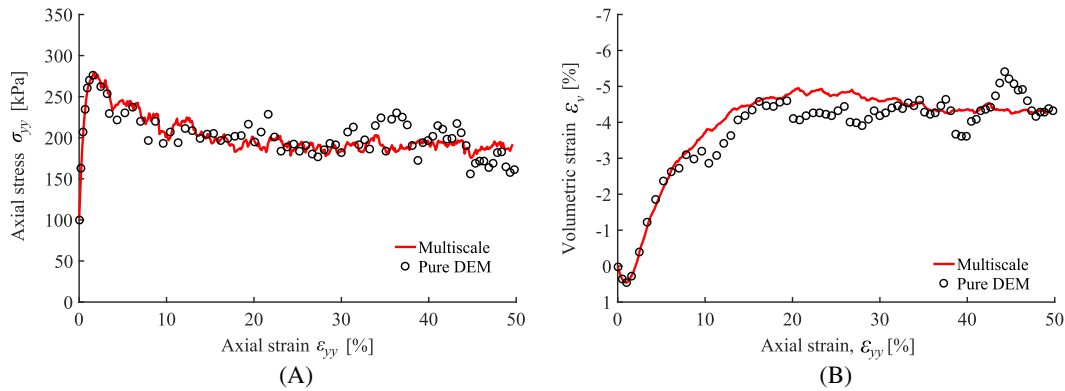


**FIGURE 4** Comparison of global stress-strain relation between material point method/discrete element method (MPM/DEM) multiscale predictions and pure DEM simulations on the same representative volume element (RVE) in a single element test: A, stress-strain relation, B, dilatancy curve [Colour figure can be viewed at wileyonlinelibrary.com]

and dilatancy curve from multiscale modeling and pure DEM modeling, showing that the multiscale predictions can accurately reproduce the complex, nonlinear response of granular materials up to large strain.

### 3.2 | Biaxial compression test

The proposed multiscale approach is further employed to simulate biaxial compression tests on a dense sand. Particular emphases are placed on the occurrence and evolution of the strain localization pertaining to the underpinning grain-scale material response. The sample also serves to explore the sensitivity of multiscale modeling to the choice of multiple model parameters, including mesh density and number of particle per cell. The model setup for the biaxial compression test is depicted in Figure 5, where we consider a sand sample with dimensions of 1 m by 2 m. Both lateral boundaries of the sample are subjected to a constant confining pressure  $\sigma_{xx} = 100$  kPa, while the bottom is totally fixed. A rough plate (with constrained movement in x and y direction) is attached to the top boundary of the sample and moves monotonically downward with a constant vertical velocity  $v = 0.02$  m/sec (the loading rate is equal to 1%/sec). The loading velocity of the rough plate is increased linearly from zero to the prescribed magnitude at the beginning to reduce the stress oscillation.

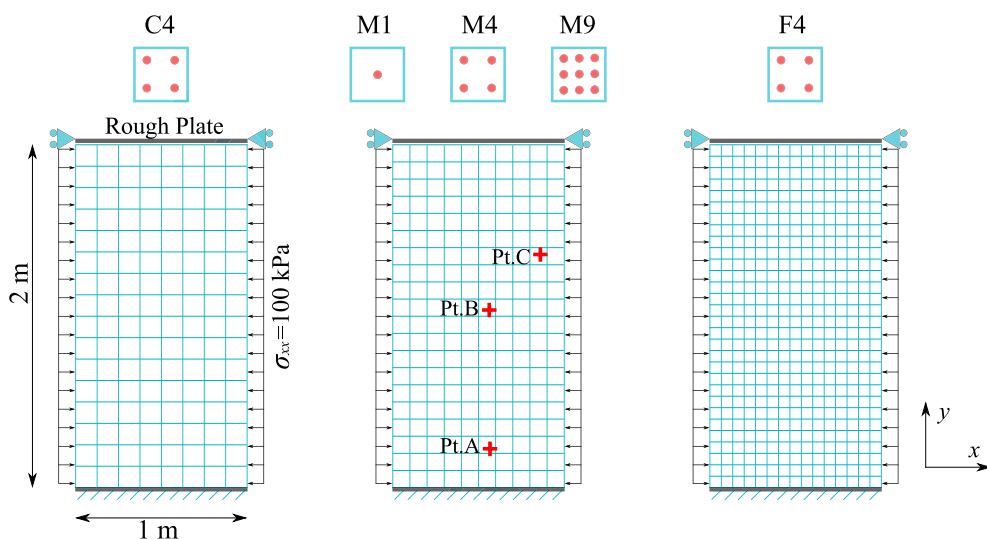


**FIGURE 5** Model setup for biaxial compression test. In each name of the five different cases, the capital letter denotes the mesh density: Coarse ( $16 \times 8$  elements), Medium ( $20 \times 10$  elements), and Fine ( $30 \times 15$  elements), whereas the second number denotes particles per cell (PPC). Pt. A, B, & C marked by red cross are locations chosen for the following meso-scale analysis [Colour figure can be viewed at [wileyonlinelibrary.com](http://wileyonlinelibrary.com)]

To study the sensitivity of mesh density and particle per cell (PPC)<sup>69,75†</sup> of MPM on the global responses, we consider the following five comparison cases: **C4, M1, M4, M9**, and **F4** (the capital letter denotes the mesh density: Coarse = ( $16 \times 8$  elements), Medium = ( $20 \times 10$  elements), and Fine = ( $30 \times 15$  elements); the number after each letter denotes the number of particles per cell used). The same RVE used in the single element test has been employed for the following biaxial compression tests. Gravity is ignored in the simulation.

### 3.2.1 | Global responses

The global stress-strain relations for all five cases are presented together with the pure DEM simulation on the RVE in Figure 6. The vertical stress  $\sigma_{yy}$  and the shear stress  $\sigma_{yx}$  are obtained by normalizing the vertical and horizontal reaction forces acting on the loading plate with the plate area. We take the case of **M4** as an example on discussion, while leaving the comparison with other cases on the sensitivity study in subsequent subsection. For Case **M4** (blue curves), it is apparent that the global responses of the sample compare well with the pure DEM simulation (denoted by empty circles in Figure 6). Indeed, the pre-peak responses of  $\sigma_{yy}$  from the multiscale modeling are almost identical with the pure DEM simulation, both showing a peak of about 280 kPa. Case **M4** reaches a peak at around  $\epsilon_{yy} = 1.6\%$ , slightly earlier than that of the DEM ( $\epsilon_{yy} = 1.7\%$ ). The post-peak response by multiscale modeling is relatively smooth, while that from pure DEM shows some fluctuations, primarily because of the limited number of particles (400) used. A steady state of  $\sigma_{yy} \approx 220 \text{ kPa}$  at  $\epsilon_{yy} = 8\%$  is predicted by **M4**. The sample again offers compelling evidence that the multiscale modeling is feasible in producing realistic sand responses. The horizontal (shear) stress  $\sigma_{yx}$  acting on the plate is highly fluctuating over the loading process, albeit its magnitude is much smaller compared with the vertical stress. Nevertheless, the fluctuations shown by  $\sigma_{yx}$  are found bearing high relevance to the formation and development of shear bands in the sample, as will be discussed in the sequel.

### 3.2.2 | Mesh and particle per cell (PPC) dependency

The multiscale MPM/DEM approach cannot escape a similar curse of mesh dependency as suffered by most mesh-based methods such as FEM. To explore how sensitive the multiscale predictions are to the mesh size and PPC number, Figure 6 presents the global responses for all five cases in comparison with the pure DEM simulations. Evidently, samples with different mesh size or PPC show almost identical pre-peak responses that are consistent with the DEM simulations. The predicted peak  $\sigma_{yy}$  values are close in all cases too. However, their post-peak responses show certain significant diver-

<sup>†</sup>Note that PPC stands as Particles Per Cell and is a historical name used in MPM, but indeed refers to the number of material points (RVEs) per grid element here to avoid confusion with the particles in a RVE.

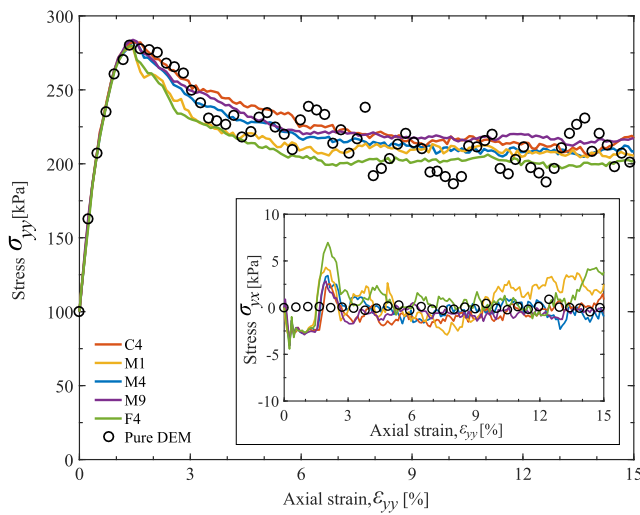


**FIGURE 6** Global stress-strain responses of sand sample subjected to biaxial compression predicted by the multiscale modeling approach for cases with different mesh density and particle per cell (PPC), in comparison with the pure DEM simulation on the representative volume element (RVE) under identical boundary conditions (denoted as empty circles). The vertical and horizontal stresses are calculated by diving the reaction forces acting on the loading plate with the plate area [Colour figure can be viewed at [wileyonlinelibrary.com](#)]

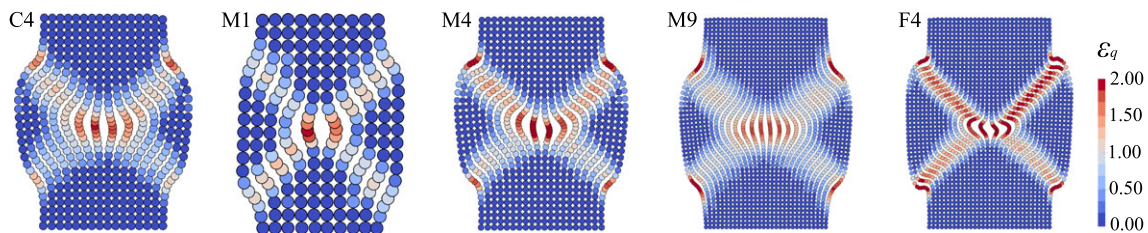


**FIGURE 7** Contour of deviatoric strain  $\epsilon_q$  for samples with different meshes and/or particle per cell (PPC) at the final state  $\epsilon_{yy} = 15\%$  under biaxial compression [Colour figure can be viewed at [wileyonlinelibrary.com](#)]

gence. For the three cases with identical PPC but different meshes (**M4**, **C4**, and **F4**), the finer mesh case generally leads to more softening post-peak responses with smaller steady state stress. For the three cases with medium mesh but different PPC (**M1**, **M4**, and **M9**), the case with a larger PPC number appears to render relatively less softening responses than those with a smaller PPC number. The responses in all three cases are between those of **C4** and **F4**, indicating that the influence of PPC on the global responses is less significant than that of the mesh density. As pointed out by Steffen et al.,<sup>75</sup> adopting a larger PPC is beneficial as it helps reduce the upper bound of the error and increase the computational stability. However, a larger PPC may also result in a substantial increase in computational cost. Therefore, both effectiveness and accuracy should be taken into consideration in selecting a proper value for PPC. Figure 7 further compares the final strain localization patterns observed in all five cases at a final state  $\epsilon_{yy} = 15\%$ . In all cases, the strain is found localized in symmetric cross-shape shear bands in the sample. The band width appears to be dependent on the mesh size, with narrower bands in cases of finer mesh. However, PPC does not show an obvious influence on the band width. A possible way to resolve the mesh dependency issue for the coupled MPM/DEM approach may follow similar techniques having been used in continuum modeling approaches, eg, by invoking nonlocal formulations<sup>49</sup> or introducing certain regularization schemes.<sup>76</sup> This is however beyond the scope of the present study and will not be discussed here. The observed differences in the five cases, nevertheless, are considered insignificant. For the rest of this subsection, Case **M4** is chosen for detailed analysis and discussion.

### 3.2.3 | Shear band evolution

Strain localization has been well reproduced in our multiscale simulation of biaxial compression. To analyse the onset and development of strain localization, we identify four representative quantities of the material responses at the three study points (Pt. A, B, & C), namely, the deviatoric strain  $\epsilon_q$ , void ratio  $e$ , the rotation angle  $\theta$ , and the displacement field  $\mathbf{u}$ ,

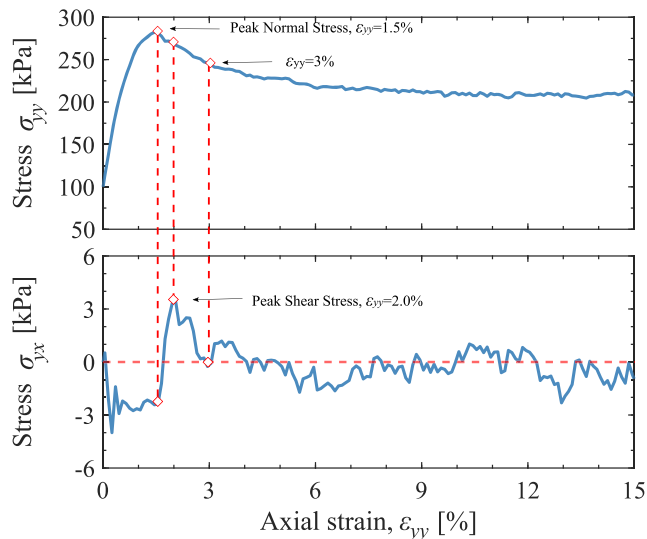


**FIGURE 8** Global stress-strain relation for Case M4 (Medium mesh, four particle per cell [PPC]) in biaxial compression test [Colour figure can be viewed at [wileyonlinelibrary.com](http://wileyonlinelibrary.com)]

and examine their evolutions at four stages of deformation (axial strain  $\epsilon_{yy} = 1.5\%$ ,  $2.0\%$ ,  $3.0\%$ , and  $15\%$ ). The results are plotted in Figure 9. The global stress-strain relations of Case M4 has also been replotted in Figure 8, for better explanation of the evolution of shear band in the sample.

As can be seen from Figure 9, the overall occurrence and development of the cross-shape shear bands in the sample resemble largely those observed from the case with random bedding plane and rough boundary in Zhao and Guo.<sup>47</sup> A dominant rightwards-tilting shear band, with an angle about  $60^\circ$  to the horizontal, is observed to develop prior to the peak normal stress at  $\epsilon_{yy} = 1.5\%$  and the resisting shear stress because of the constraint by the rough top plate points to the left (negative in value) (Figure 8). The shear deformation and anti-clockwise rotations in the rightward-tilting band are apparently larger than the rest of the sample. When the peak normal stress state is reached, the shear stress exerted by the plate dramatically changes from negative (pointing to the left) to a positive (pointing to the right) peak at around  $\epsilon_{yy} = 2.0\%$ , which further enhances the development of the first band and brings the second shear band (leftward-tilting) to be more intensive. After  $\epsilon_{yy} = 2.0\%$ , both normal and shear stresses gradually drop, while both shear bands continue to develop until the final state. Notably, the leftward-tilting band develops clockwise rotations which gradually cancel out the positive rotations by the rightward-tilting band at the center of the sample, leading to the final rotation negligibly small at the sample center. However, both the shear strain and dilatant volumetric strain are greatly enhanced at the center due to development of both bands. The observations are consistent with the FEM/DEM simulations in the study of Zhao and Guo.<sup>47</sup> When the loading approaches the final state at  $\epsilon_{yy} = 15\%$ , the cross-shape shear bands develop in their full. The displacement field of the sample can be divided into four distinctive portions by the cross-shape shear bands: the two side triangle parts moving down and laterally, the upper pentagon part moving downwards, and the lower pentagon part with only negligible movements. The contour of void ratio clearly showed the dilative deformation of material within shear band (note that the initial void ratio is 0.177). The final rotation inside the shear bands can reach as large as  $58^\circ$ . Under this circumstance, severe mesh distortion would have been inevitable for conventional FEM, and thus accuracy and effectiveness cannot be guaranteed.

### 3.2.4 | Meso-scale analysis

The proposed multiscale modeling approach enables us to probe the underlying microstructural mechanisms for macroscopic observations, through the RVEs employed as a meso-scale structure bridging the micro and macro scales of a problem. Herein, we chose three points inside the sample to conduct a meso-scale analysis (their positions are shown in Figures 5 and 9), whereby Point A is located at the bottom part of the sample and is far away from the shear bands, Point B is located at the center of the sample and also the interception of the two shear bands and, Point C is at the upper part of the sample and is inside the rightward-tilting shear band (see also the left figure in Figure 9D). The local responses for these three points and their microstructures at final state are shown in Figures 10 and 11, respectively.

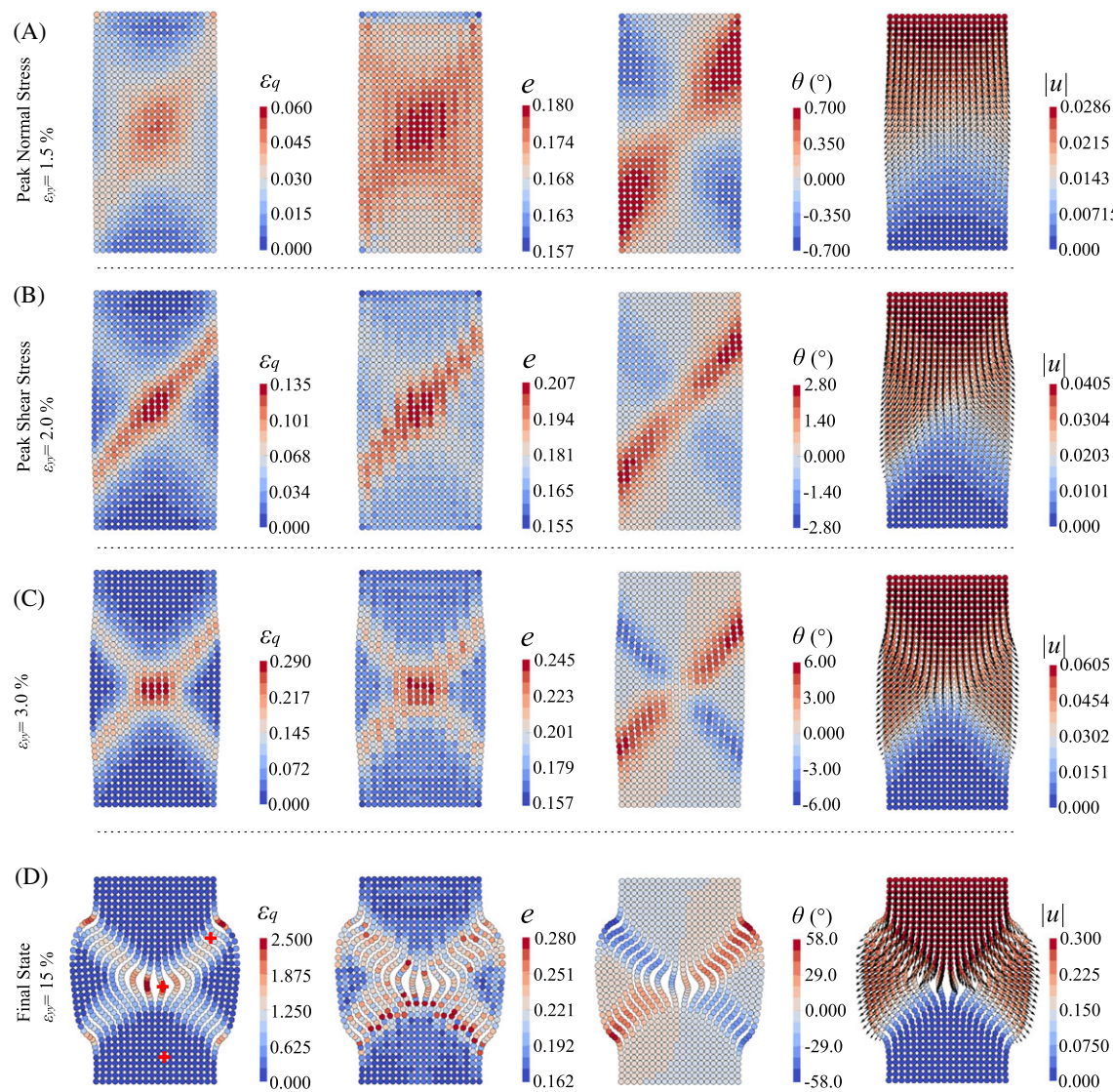


**FIGURE 9** Shear band evolution for Case M4 in biaxial compression test [Colour figure can be viewed at [wileyonlinelibrary.com](http://wileyonlinelibrary.com)]

### Point A

Point A is outside the shear bands at the bottom part of the sample. Apparently, it only develops a small peak deviatoric stress at ( $\epsilon_q \approx 1\%$ ) before undergoing unloading. Rather low fabric anisotropy ( $F_a \approx 0.075$ ) has been induced at this point. The effective stress path in Figure 10B clearly confirms that Point A undergoes a perfect loading and unloading process. Being outside the shear bands, this point experiences marginally small rotation ( $\theta = -0.1^\circ$ ) and relatively small volume change. The above observation is further confirmed by the contact force chain network shown in Figure 11A, which shows the deformation of RVE at Point A is almost negligible and its initial isotropic structure is well preserved.

### Point B

Point B is located at the lower center of the cross-shape shear bands. Its behavior is significantly influenced by the evolution of both bands. Point B first shows a monotonic increase in stress before strain localization occurs at a global vertical strain of  $\epsilon_{yy} = 1.5\%$  (peak normal stress state), from which its deviatoric stress,  $q$ , drops rapidly because of the development of the first dominant shear band, which induces strain softening. The stress drop is reversed when the second shear band starts to develop before the global shear stress reaches its peak at  $\epsilon_{yy} \approx 2.0\%$ . Later, the sample domain is restored to an approximately symmetric field in terms of shear deformation. The symmetry in deformation pattern, together with the rough boundary, apparently help the center point sustain a large stress state ( $p_{peak} \approx 420$  kPa,  $q_{peak} \approx 150$  kPa) until this symmetry breaks at  $\epsilon_{yy} \approx 8.5\%$ . After the breakage of symmetry, both  $p$  and  $q$  gradually decrease, and Point B rotates

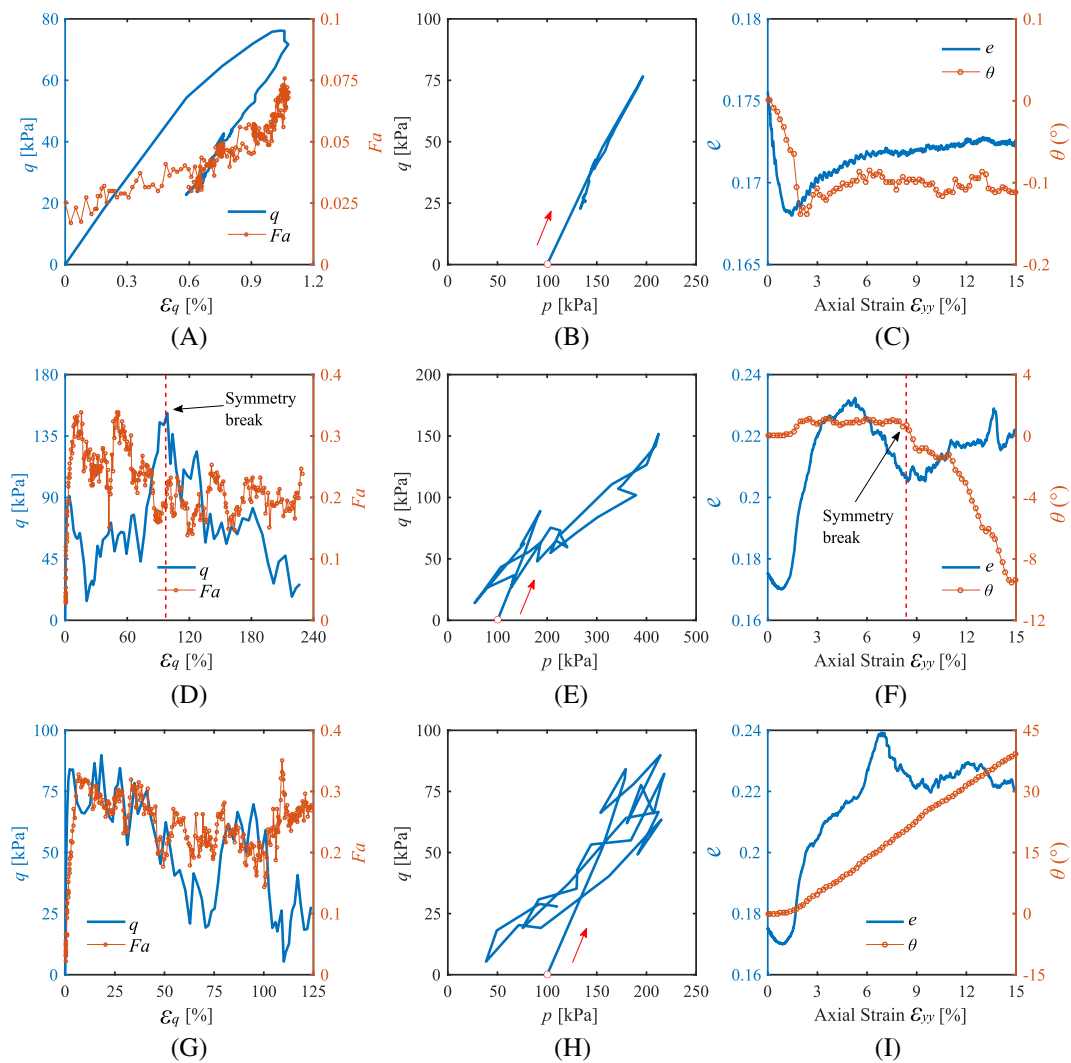


**FIGURE 10** Local responses for selected material points in biaxial compression test: (A-C) Point A, (D-F) Point B, and (G-I) Point C [Colour figure can be viewed at [wileyonlinelibrary.com](http://wileyonlinelibrary.com)]

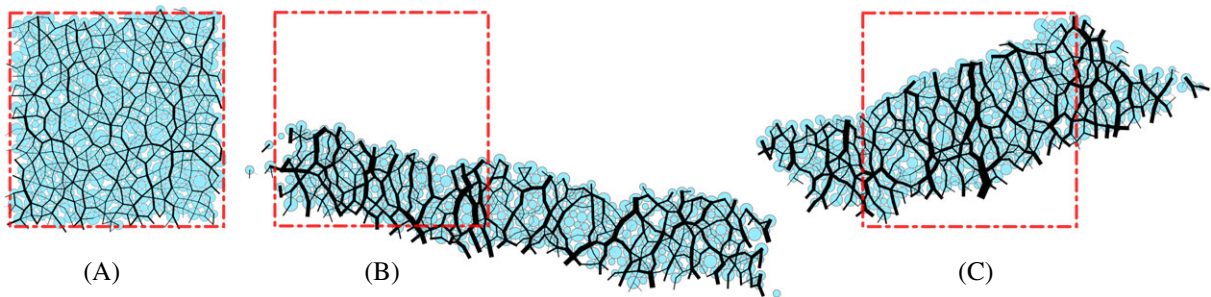


**FIGURE 11** Force chain for selected material points in biaxial compression test: (A) Point A, (B) Point B, (C) Point C. The dashed line indicates their undeformed shape [Colour figure can be viewed at [wileyonlinelibrary.com](http://wileyonlinelibrary.com)]

clockwise by a mild rotation angle ( $\theta = 10^\circ$ ). The  $F_a$  exhibits an increase to a double-peak evolution with much fluctuations, but its range of fluctuation remains between 0.2 to 0.3. As can be seen in Figure 10F, the initial contraction at elastic stage, dilation because of occurrence of shear bands, and second contraction/dilation before/after the breakage of symmetry are well recorded, reflecting complex loading Point B has undergone. The strong force chain and apparently deformed RVE with a mild rotation shown in Figure 11B is consistent with the observation from Figure 10D-F.

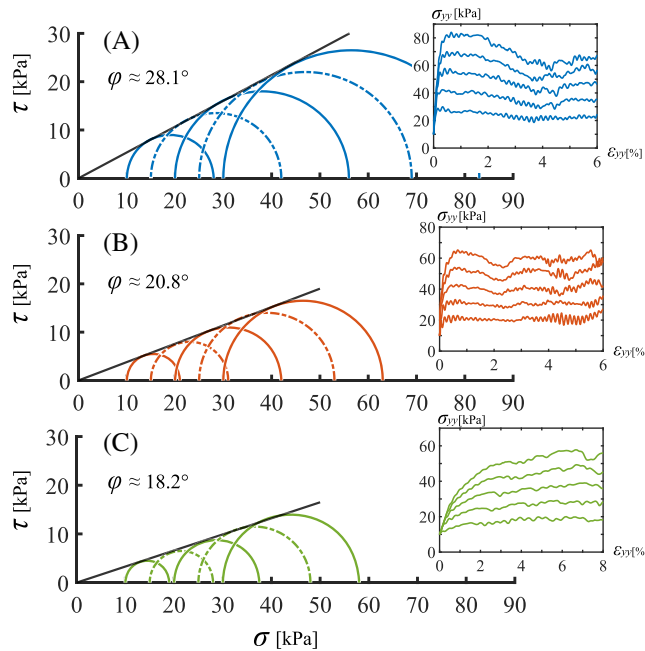


**FIGURE 12** Estimation of the macroscopic friction angle for each case of representative volume element (RVE) used in the footing problem: A, Dense, B, Medium Dense, and C, Soft soils [Colour figure can be viewed at [wileyonlinelibrary.com](http://wileyonlinelibrary.com)]

### Point C

Point C is located inside the rightward tilting shear band in the upper right part of the sample. The stresses at Point C shows a rapid increase to a peak and then drops (with fluctuations) with the continuous development of the shear band. The evolution of  $F_a$  at Point C is similar to that of Point B, reaching a peak first then dropping with fluctuations. The final force chain network of the RVE at Point C (Figure 11) indicates considerable shear deformation occurs at this point. Point C begins to experience a steady rotation right after the peak stress state until the final state, amounting to final rotation of  $38^\circ$ . The large rotation it undergoes is further confirmed by the observation of force chain network in Figure 11C.

### 3.3 | Rigid footing

We further consider a classic geotechnical problem—a strip rigid footing penetrating into a weightless soil foundation. Modeling of rigid footing problem is widely considered challenging as it may involve large deformation of soil when the penetration is deep. It is difficult for conventional updated Lagrangian FEM to handle as the soil elements at the bottom edge of the footing, commonly regarded as a singular plasticity point,<sup>77</sup> may be severely distorted during the FEM calculation which frequently gives rise to convergence issue (readers can refer to Figure 13 in Nazem & Sheng<sup>78</sup> for deformed mesh in footing problem). It will demonstrate in the following that the proposed MPM/DEM approach can readily handle this situation. Moreover, we demonstrate that multiple failure modes observed in rigid footing, namely, general shear failure, local shear failure and punching failure modes, can be captured by the MPM/DEM simulations.

#### 3.3.1 | Packing preparation and model setup

To model the three failure modes, three RVEs, dense, medium dense, and soft packing,<sup>‡</sup> are generated based on the parameters listed in Table 2. The dense and medium dense packing differ only in their initial void ratios,  $e_0$ , to represent dense and medium dense foundation soils, respectively. In order to model a soft soil foundation, where punching failure may occur, the soft packing uses reduced Young's modulus  $E$ , interparticle friction angle  $\varphi$ , and dimensionless parameter  $\eta$  compared with the dense packing case to have a reduced contact stiffness. It is noteworthy that the rolling resistance mentioned in Section 2.2.1 is taken into account to generate RVEs with more realistic strengths.

<sup>‡</sup>In DEM, it is difficult to generate extremely loose, stable packings without special techniques such as those used in Wu et al.<sup>51</sup> Alternatively, we elect to prepare a packing with lower overall stiffness and strength to represent soft soils in this study. This soft packing is complementary to the dense and medium dense packings to generate a comprehensive spectrum of failure modes observed in footing foundation.

**TABLE 2** Model parameters for three different representative volume elements (RVEs) used in multiscale modeling of rigid footing problem on dense, medium dense, and soft soil foundations

Name	Particle Num.	r(mm)	$\rho(\text{kg/m}^3)$	E (MPa)	$\nu$	$\varphi(^{\circ})$	$\beta$	$\eta$	$\alpha$	$e_0$
Dense	400	3-7	2650	800	0.5	23	1.0	0.05	0.1	0.1874
Medium Dense	400	3-7	2650	800	0.5	23	1.0	0.05	0.1	0.2314
Soft	400	3-7	2650	80	0.5	20	1.0	0.02	0.1	0.2299

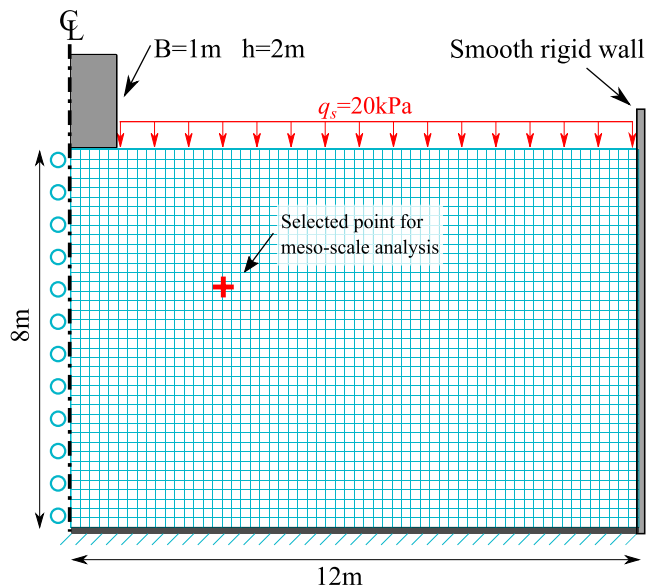


**FIGURE 13** Model setup for the footing problem where the footing has a rough surface and the right-side wall is rigid and smooth to allow only vertical movements of soil in contact [Colour figure can be viewed at [wileyonlinelibrary.com](http://wileyonlinelibrary.com)]

Macroscopic effective friction angles of the generated RVEs are needed for computing the analytical bearing capacity, in order for comparison with the multiscale modeling. To this end, biaxial compression tests are carried out on each RVE under five confining pressures, 10 kPa, 15 kPa, 20 kPa, 25 kPa, and 30 kPa. From the corresponding stress-strain responses (insets of Figure 12), the Mohr circles of the peak stress states are plotted in Figure 12. The corresponding macroscopic effective friction angles for dense, medium dense, and soft packing are then estimated as  $28.1^{\circ}$ ,  $20.8^{\circ}$ , and  $18.2^{\circ}$ , respectively. The three RVEs are assigned to the material points in three identical MPM domains shown in Figure 13 for the following simulations and modeling.

The geometry, boundary conditions, and loading scheme for the rigid footing problem are shown in Figure 13. The soil domain is 12 m wide and 8 m deep, while the rigid footing foundation has a dimension (width  $\times$  height) of 1 m  $\times$  2 m. The whole soil domain is discretized into  $108 \times 72 = 7776$  elements with an element size of 0.11 m. In order to improve the mesh resolution without significantly increasing the computational cost, an initial value of PPC of 1 is adopted. Note that the whole domain includes a total of 7776 RVEs, and each of them contains 400 particles, which amounts to a total of 3 110 400 particles to be handled in each loading step. A smooth wall is placed at the right boundary of the soil to constrain its horizontal movement. The left boundary is a symmetric plane, while the bottom is totally fixed. The surface of the rigid footing is rough. A constant, uniform surcharge  $q = 20$  kPa is applied to the ground surface, except the resting area of the footing. The settlement of the footing is modeled by prescribing a constant downward velocity 0.1 m/sec on it. A simulation is terminated when a maximum settlement  $d/B = 1.5$  is reached. Gravity is neglected here.

### 3.3.2 | Failure patterns

Three distinctive failure patterns are observed in our multiscale modeling of the soil foundations under rigid footing penetration. They resemble the modes of general shear failure, local shear failure, and punching failure, respectively. The contours of deviatoric strain  $\epsilon_q$ , displacement  $\mathbf{u}$ , void ratio  $e$ , and cumulative rotation  $\theta$  at the final failure state for all three cases, are plotted in Figures 14 and 15. In analyzing the failure patterns, we wish to highlight the competition between two array of curvilinear slip line caused by the footing penetration in the soil. The first array (hereafter referred

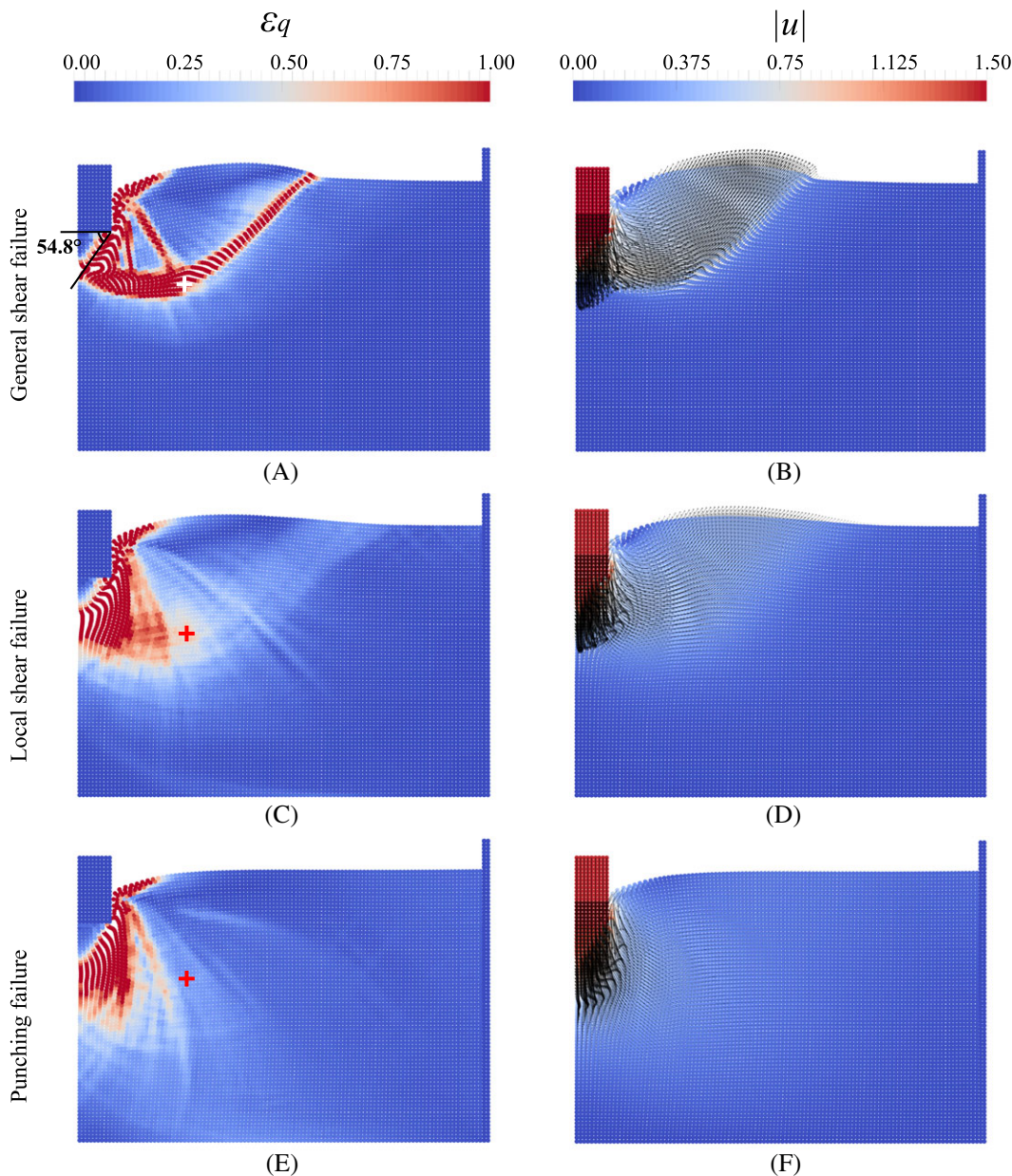


**FIGURE 14** Contour of deviatoric strain  $\epsilon_q$  and displacement field  $\mathbf{u}$  for cases using different representative volume element (RVEs) at final state  $d/B = 1.5$  in footing problem [Colour figure can be viewed at [wileyonlinelibrary.com](http://wileyonlinelibrary.com)]

to as Array A) of slip lines emanate from the outer edge and bottom corner of the footing, pointing right-downwards. The second array of slip lines (Array B) originate from the tip and surface of the triangle wedge underneath the footing, pointing right and upwards. The curvilinear slip lines in the two arrays are orthogonal, as can be clearly seen from the shear strain contours in Figure 14.

#### General shear failure

Our multiscale simulation on the footing with the dense packing shows a general shear failure mode, as shown in Figures 14A and 14B and Figures 15A and 15B. The failure pattern can be defined by four primary slip lines clearly identifiable from Figure 14A. Three of them, emanating from the outer edge of the footing and pointing downwards to the left, vertical, and right, respectively, belong to Array A. The downward left-tilting slip line and the footing bottom form an approximate rigid triangular wedge (or active Rankine zone as termed by Terzaghi<sup>79</sup>). The fourth major slip line originates from the tip of this wedge and extends curvilinearly right and upwards, belonging to Array B. Apparently, this Array B slip line is the most dominant one, intercepting all previous three in Array A and defines the failure mode. It partners

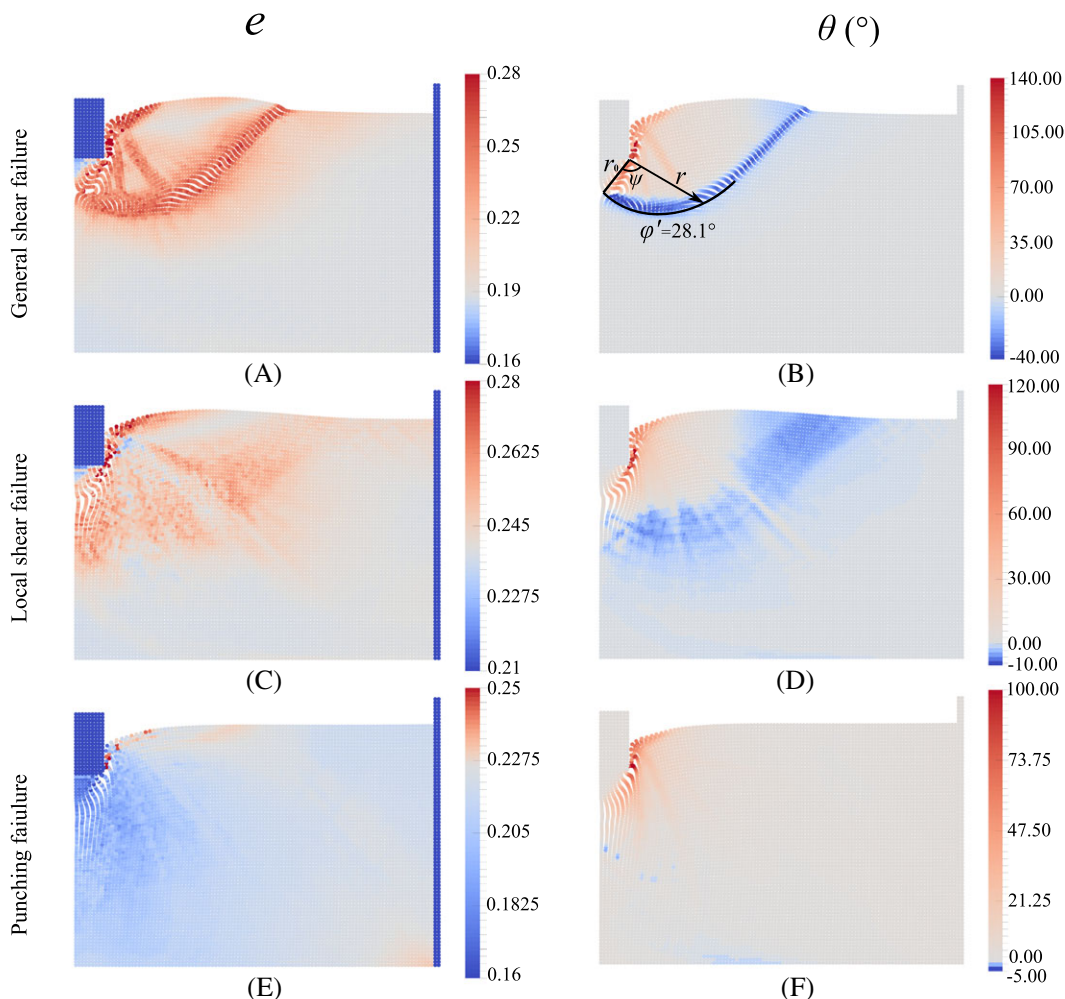


**FIGURE 15** Contour of void ratio  $e$  and rotation  $\theta$  for cases using different RVEs at final stage  $d/B = 1.5$  in footing problem. White represents corresponding initial void ratio in void ratio contour (A,C,E), and denotes zero rotation angle in rotation contour (B,D,F) [Colour figure can be viewed at [wileyonlinelibrary.com](http://wileyonlinelibrary.com)]

with the wedge-edge shear band and the downward right-tilting one in Array A form a radial shear zone, the bottom of which presents approximately a log-spiral curve. Immediate next to the right, the extended long part of this dominant Array B slip line and the right Array A slip line form a major failure zone of the largest volume extending to the ground surface. This last failure zone is commonly termed as the Rankine passive zone in the literature.<sup>79</sup> The overall failure configuration is indeed consistent with the Terzaghi's description on the failure mode. The middle Array A slip line does not appear to play a major role in the zonation, but simply subdividing the radial shear zone into two portions. From the contour of displacement vector in Figure 14B, one can clearly observe that the soil immediately under the footing foundation is pushed downward, acting as if it were a part of the foundation while the surrounding soil is dispelled alongside. The dense packing of the soil renders the deformation and mobilization of soil far reaching, forming an apparent heave as wide as around 2.5 times of the footing width at the ground surface.

Indeed, rather consistent characteristic of failure modes is also captured by the contour of void ratio  $e$  and rotation angle  $\theta$  shown in Figure 15. The void ratio of soil within all slip lines shows an apparent increase because of shear dilation (note that in Figure 15A, 15C, and 15E, white represents initial void ratio  $e_0$ , whereas red and blue represent dilation and contraction, respectively). Moreover, the particles inside the dominant Array B shear band show clockwise rotations, while those within three Array A slip line rotate anticlockwise (note that in Figure 15B, 15D, and 15F, white represents no rotation, whereas red and blue represent rotating anticlockwise and clockwise accordingly). These observations are consistent with those from experiments<sup>80</sup> and other numerical simulations.<sup>50</sup>

According to Prandtl's solution, the lower boundary between the triangular wedge and the radial shear zone inclines at  $\frac{\pi}{4} + \frac{\varphi'}{2} = 59.05^\circ$  to the horizontal plane. As shown in Figure 14A, the corresponding angle obtained from our simulation is

54.8°, which is slightly smaller than the analytical prediction. This discrepancy is probably because of the friction between the rough footing and soil, which prevents the soil within the triangular wedge spreading horizontally.<sup>79</sup> Notably, Prandtl's solution assumes the footing bottom is smooth.

Also, in general shear failure, the log-spiral slip line can be described by following equation:

$$r = r_0 e^{\psi \tan \varphi'}, \quad (44)$$

where  $r$  is length of line connecting the center of log-spiral curve which is the bottom corner of the footing with the points on the curve,  $r_0$  is the length of lower boundary of the triangular wedge,  $\psi$  measures the direction from  $r_0$  to  $r$ . The log-spiral slip surface with an effective friction angle  $\varphi' = 28.1^\circ$ , which is obtained in Section 3.3.1, is also plotted in Figure 15B. As can be seen, the simulation result agrees perfectly well with the analytical prediction.

### Local shear failure

The footing case with medium dense packing gives rise to a local shear failure mode. The local shear failure also exhibit a smaller triangular rigid wedge formed immediately under the footing foundation, a curved shear failure zone and small heaved ground surface. The major failure zone is the radial shear zone which is confined not far from the footing, which is considered "locally." Unlike the general shear failure, only one major Array A slip line is formed along the wedge surface, with two other under-developed Array A bands appearing next to it on the right. No mature Array B slip lines are found, but orthogonal curvilinear slip lines from both arrays are apparent in the soil foundation. The slip lines in Array B are mostly intercepted and confined by the three Array A slip lines, thus no apparent failure surface is extended to the ground surface. The intensities of both shear strain and rotations are smaller than in the general shear failure case, and the heaving height is smaller too. Dilatant zones are scattered in the mobilized soil but do not form apparent dilatant shear bands. The rotation zone is much less concentrated than the general shear failure case.

### Punching failure

Punching failure is found in the footing case using the soft packing. In contrast to aforementioned two failure modes, no Array B slip lines are developed at all. All major slip lines observed belong to Array A, which extend downward far-reaching deeper to the soil than the previous two cases. The influence zone by the footing is largely confined within a relative small region under the footing foundation. The soil immediately under the footing experiences pure compression (note that contraction of soil is shown in blue in Figure 15E), while the soil close to the wedge and footing edge exhibit large shear deformation. The slip lines that can potentially develop into Array B are all intercepted by Array A slip lines. The displacement field in Figures 14F clearly depicts the locally occurred failure. The ground surface hardly feels the failure except slight settling adjacent to the footing. Only slight anticlockwise rotations along the wedge surface and footing edge are recorded in Figure 15F.

### 3.3.3 | Analytical bearing capacity

The bearing capacity is a key design index for foundations. Prandtl<sup>81,82</sup> proposed the following analytical solution to calculate the ultimate bearing capacity  $p_u$  for a shallow footing seated on a weightless cohesionless soil in the case of general shear failure:

$$p_u = q_s N_q, \quad (45)$$

where  $N_q$  is the bearing capacity coefficient because of surcharge, and can be determined from the effective friction angle  $\varphi'$ :

$$N_q = \tan^2 \left( \frac{\pi}{4} + \frac{\varphi'}{2} \right) e^{\pi \tan \varphi'} \quad (46)$$

Although there is no available analytical solution for local shear failure and punching failure, Terzaghi<sup>79</sup> suggested using the same equation but with a reduced friction angle  $\varphi'_r$  to find the approximated bearing capacity coefficient  $N'_q$ :

$$\varphi'_r = \arctan \left( \frac{2}{3} \tan \varphi' \right) \quad (47)$$

Figure 16 shows the variation of normalized settlement with normalized ultimate loads for three cases, in comparison with the corresponding analytical solutions. The general shear failure mode shows a clear peak, followed by softening load-settlement curve, while general hardening curves are observed in the other two failure modes. As indicated in

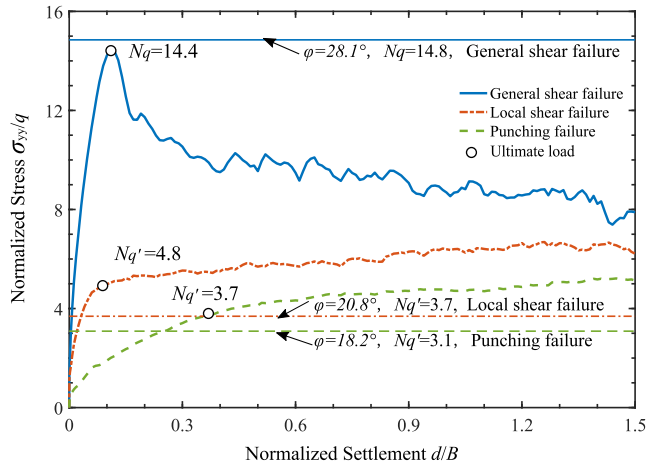


**FIGURE 16** Comparison of the bearing capacity between multiscale prediction and analytical solution on a rigid footing problem. The bearing capacity of multiscale study is computed at their ultimate load point, a point where the slope of the load-settlement curve first reaches 0 or steady and minimum value.<sup>82</sup> The analytical prediction is computed from the macroscopic friction angles mentioned at Section 3.3.1 [Colour figure can be viewed at [wileyonlinelibrary.com](http://wileyonlinelibrary.com)]

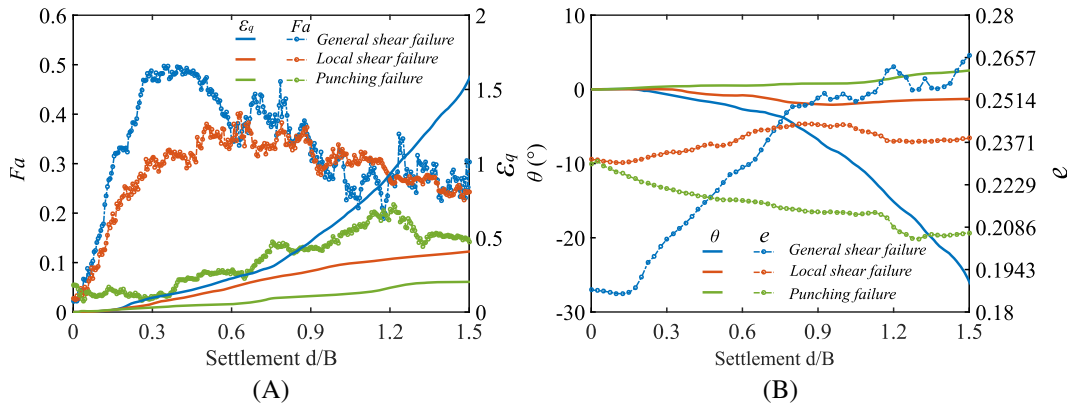


**FIGURE 17** Local response for material points chosen from different cases in footing problem [Colour figure can be viewed at [wileyonlinelibrary.com](http://wileyonlinelibrary.com)]

Figure 16, the analytical bearing capacity coefficients, based on macroscopic friction angles estimated from Figure 12, are 14.8, 3.7, and 3.1 for general shear failure, local shear failure, and punching failure, respectively. The predicted values by our MPM/DEM multiscale approach are 14.4, 4.8, and 3.7, respectively, for the three cases. The analytical and numerical predictions are close, except in the case of local shear failure. The local shear failure mode observed in this study may actually be a transitional failure mode between the general shear failure model and true local shear failure mode, resulting in a relatively larger value for the predicted bearing capacity than the analytical one.

### 3.3.4 | Meso-scale analysis

To analyse the local behavior for the above three cases, a reference point from the same location is chosen for all three cases (the location of the chosen point is marked as a cross in Figures 13 and 14). The evolutions of the deviatoric strain  $\epsilon_q$ , fabric anisotropy  $F_a$ , void ratio  $e$ , and rotation angle  $\theta$  against the normalized settlement  $d/B$  are presented in Figure 17. In all three cases, the deviatoric strain  $\epsilon_q$  increases monotonically with the footing penetration, where the general shear failure mode shows a power law increase before it reaches a final value of 1.6 at the end of the penetration, indicating an uncontrollable speeding shear failure of the foundation. In both the local and punching shear failure modes, the increase of  $\epsilon_q$  with footing settlement is almost linear, leading to much smaller final deviatoric strains of 0.4 and 0.22, respectively, than the general shear failure mode. The evolutions of both void ratio  $e$  and rotation  $\theta$  are consistent with the observation on  $\epsilon_q$  for the three cases. The above observation is consistent with the fact that the chosen material point lies in the main

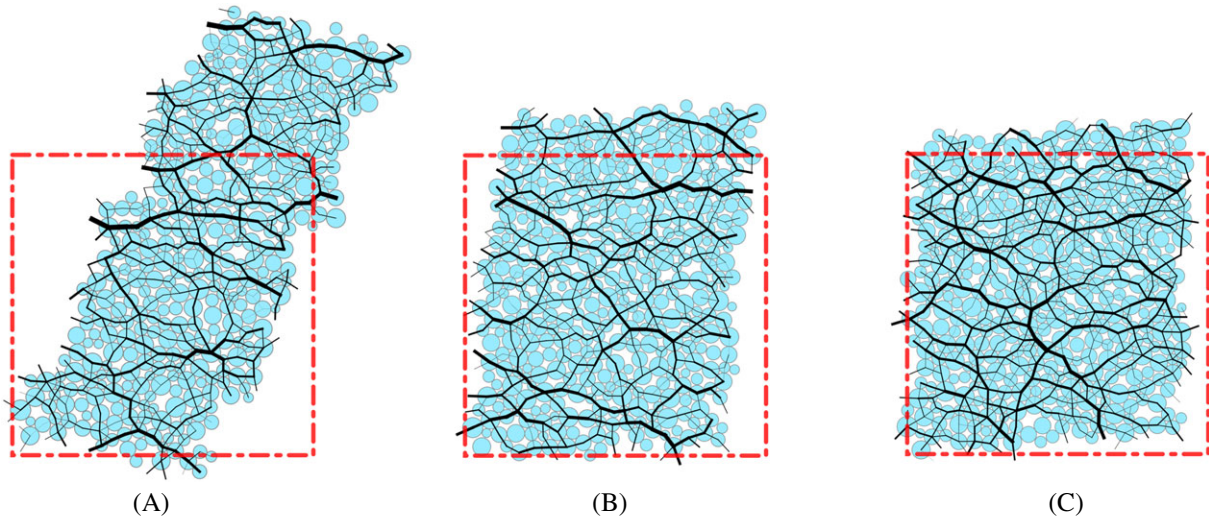


**FIGURE 18** Force chain for material points chosen from difference cases in footing problem: A, General shear failure, B, Local shear failure, and C, Punching failure. The dashed line indicates their undeformed shape [Colour figure can be viewed at [wileyonlinelibrary.com](http://wileyonlinelibrary.com)]

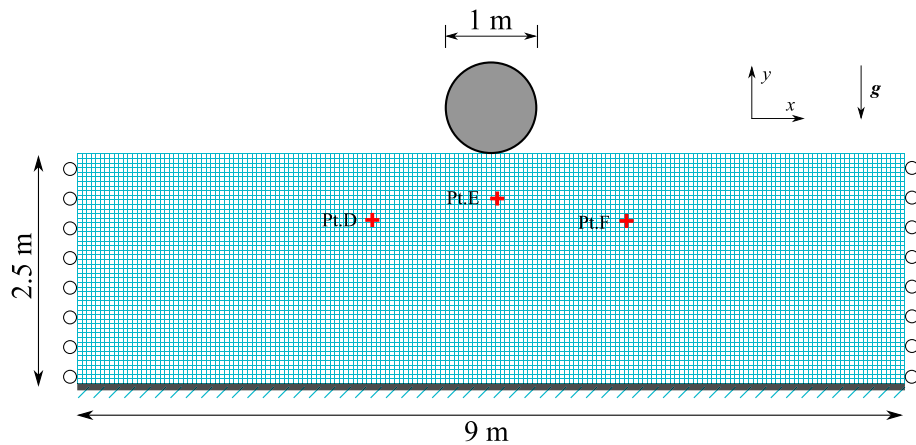
slip surface for the general shear failure case, whereas it is located close to a partially developed failure surface for the local shear failure case and outside the failure zone at all for the punching failure mode. Indeed, for the punching failure mode, the representative material point lies outside the punching shear wedge and undergoes contraction only, evidenced by the smaller deviatoric strain and decreased void ratio during the penetration of the footing in Figure 17. The fabric anisotropy at the chosen points experience an initial increase to peak followed by a softening to relatively steady state for both general and local shear failure modes, whereas it remains a rather small value for the punching failure.

Figure 18 further compares the force chain networks of the selected material points at the final state in the three cases. Evidently, a combined shear-compression deformation is found for the point in the general shear failure case, resulting strong loading bearing structure approximately along the horizontal direction and large clockwise rotations. Both shear deformation and rotations shown by the contact force network are much less in the local shear failure mode. As for the punching failure case, the material point experience negligibly small deformation and rotation, resulting in an almost isotropic contact force network, which confirms early observation of low fabric anisotropy for this case. Overall, the observations from the contact force network are consistent with those from Figure 17 as well as the global behavior of the footing problem.

### 3.4 | Pipe-soil interaction

This subsection presents a more complex example, where large deformation analysis is essential. The installation and maintenance of pipelines are of significant engineering importance for offshore energy extraction and transport and seabed communication fiber cables.<sup>83</sup> Under various working loads (eg, gravity, wave, and earthquake), an offshore seabed pipeline may experience significant vertical and lateral displacement during and after its installation, causing complicated soil-pipe interactions involving large deformation. For safe design and reliable maintenance, it is critical to assess the large deformation behavior of the supporting soil interacting with the pipeline.

The soil-pipe interaction problem to be considered in this study is shown in Figure 19. We consider a soil domain of 9 m wide and 2.5 m deep. The bottom of the soil domain is fixed in both directions while the side edges are only constrained horizontally. A rough pipe of a diameter of 1 m is released to settle from above the center line of the soil domain and penetrate into the soil vertically for 0.8 m (measured by bottom of the pipe) first, and is then moved horizontally to the left for 0.7 m. The loading scheme is depicted by the velocity profile and coordinate change of the pipe bottom (inset) in Figure 20. The loading scheme has considered a balance of accuracy and efficiency: the velocity is chosen small enough to ensure the quasi-static condition can be loosely satisfied, while it is chosen as large as possible to shorten the computational time. A smaller horizontal velocity is adopted to ensure there is sufficient time for the soil behind the pipe to rearrange. Adding the accelerating/decelerating ramps in the loading scheme helps to alleviate the stress oscillations during the computations. The entire soil domain is discretized with 9800 elements, with one particle (one PPC) considered in each element. In this problem, we adopt the same dense packing used in footing problem (Section 3.3) to serve as the



**FIGURE 19** Model setup for the soil-pipe interaction problem. Selected particles for meso-scale analysis is marked as red cross [Colour figure can be viewed at [wileyonlinelibrary.com](http://wileyonlinelibrary.com)]

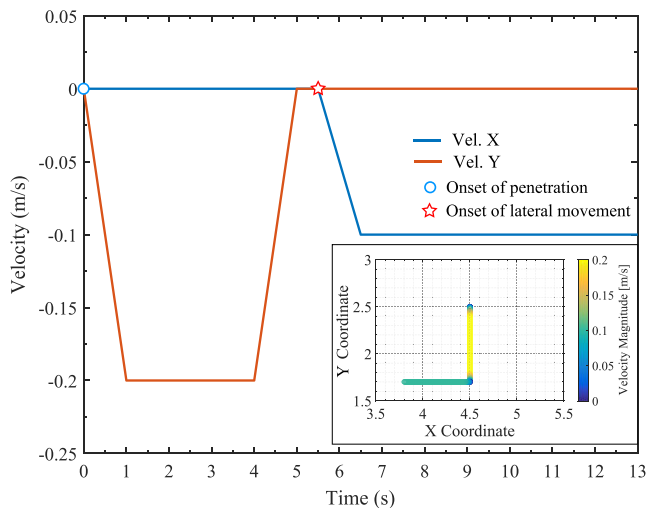


**FIGURE 20** Prescribed velocity for the pipe in soil-pipe interaction problem [Colour figure can be viewed at [wileyonlinelibrary.com](http://wileyonlinelibrary.com)]

RVE. Before applying any pipe-induced deformation, the soil is considered to be loaded by gravity and the RVEs to be assigned are isotropically compacted in the DEM solver to their corresponding geostatic pressure:  $p = \rho gh$ , where  $g$  is gravity and  $h$  is the depth of each material point.

### 3.4.1 | Global responses

The reaction force of soil acting on the pipe is plotted in Figure 21. To facilitate explanation, the whole loading process is divided into two parts to discuss: the (vertical) penetration stage and the lateral movement stage. In the penetration stage, the horizontal reaction remains low, while the vertical reaction force gradually increases to a peak of 250 kN towards the end of the penetration stage. Moderate fluctuations are observed in the curve, possibly because of the stress wave reflection. The depth of soil domain adopted here is 2.5 times of the pipe diameter, which is relatively shallow. The stress wave induced by penetration may not be fully dissipated in such short propagation distance. Special treatments, such as using an absorbed boundary at the bottom<sup>78</sup> or averaging the results over certain period,<sup>17</sup> could help to obtain a smoother reaction-time curve. At the end of the vertical penetration, the pipe experiences a sudden drop in vertical reaction force from its peak. When the pipe starts to move horizontally, the vertical reaction gradually drops and stays at a steady value of 25 kN, while the horizontal reaction force rapidly increases to 50 kN and maintains a slight increase thereafter. This mild increase is largely attributed to the growth of soil berm accumulated ahead of the pipe. Our simulation results agree qualitatively with that reported in Zhang et al.<sup>9</sup>

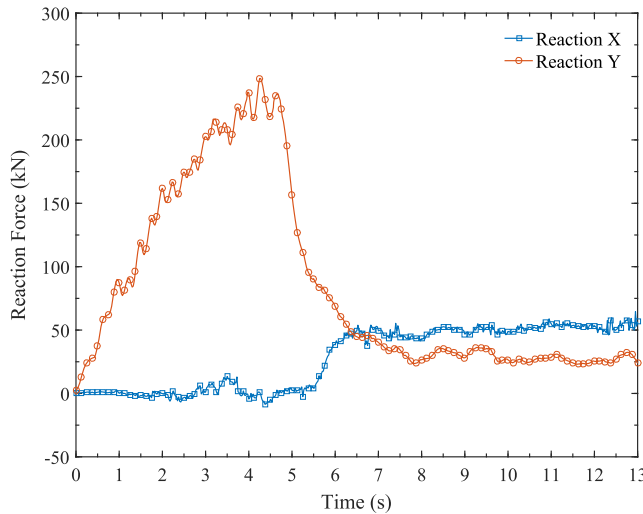


**FIGURE 21** Reaction force acting on the pipe in soil-pipe interaction problem [Colour figure can be viewed at [wileyonlinelibrary.com](http://wileyonlinelibrary.com)]

Apart from the reaction force, we have also examined the deformation pattern of the soil. Figure 22 shows the soil responses with the pipe movement in the soil, in terms of deviatoric strain and displacement. When the pipe penetrates to a depth of 0.4 m (Figures 22C and 22D), two clear shear bands originated from the bottom of the pipe extend laterally to both sides and propagate towards the ground surfaces, forming two branches of shear zones. The soil within these shear zones is mobilized and pushed aside of the pathway of the pipe. It is interesting to observe that the two branches of shear bands are not symmetrical, although the loading and boundary conditions are totally symmetrical. Possible factors accounting for the phenomenon may include the intrinsic non-coaxiality of the RVE<sup>43</sup> and the spontaneous occurrence of strain localization as a bifurcation problem. As the pipe continues to move downward, the soil is pushed laterally and upward along the shear bands, leading to the formation of heaves at the ground surface (Figure 22F). Notably, from Figure 22C and 22E, the shear band pairs around the pipe are interlayered by relatively less deformed pair zones during the vertical penetration. The heave surface on the ground surface also show changed curvatures because of the interlayer structure. It is worth noting that the shear bands on the left of pipe is lower in intensity but larger in amount. The displacement field exhibits a roughly symmetric butterfly shape pattern during the vertical penetration process.

Once the pipe begins to move left, the relatively symmetric displacement field is broken (Figure 22H). The laterally moving pipe pushes the soil in front and further intensifies the already formed shear bands in the penetration stage, leading to wider, more concentrated shear zones on the left of the pipe. The existing shear bands are also further widened while the interlayered elastic zones are greatly reduced, forming a higher soil berm pushed up by the pipe. Meanwhile, the soil on the right side of the pipe exhibits reversed displacement. This cause unloading and reverse loading for soils immediately on the right of the pipe, causing the decay of partial disappearing of the middle shear band. The ground heave formed during the first stage is gradually reduced. Meanwhile, the top shear band is developed deeper to occupy part of the original middle shear band, while the bottom shear band remains largely the same during the horizontal movement of the pipe.

### 3.4.2 | Meso-scale analysis

We again chose three points (labeled D, E, and F) to examine the local responses, where Point D/F is located inside the left/right dominant shear band and Point E is underneath the pipe (Figure 22E). Their initial position, evolution of displacement together with trajectories are depicted in 23, while their local responses are plotted in Figure 24.

#### Vertical penetration stage

In the vertical penetration stage, Point D and Point F show a similar response. Both points are pushed laterally upward by a comparable magnitude ( $\approx 0.08\sqrt{2}$  m). Since both points are inside a shear band, they exhibit an increase in both  $\epsilon_q$  and rigid rotation  $|\theta|$ . In particular, Point D rotates anticlockwise while Point F rotates clockwise. However, both  $\epsilon_q$  and  $|\theta|$  for Point D are smaller than Point F as the intensity for the left shear band is relatively lower (note that the pentagram

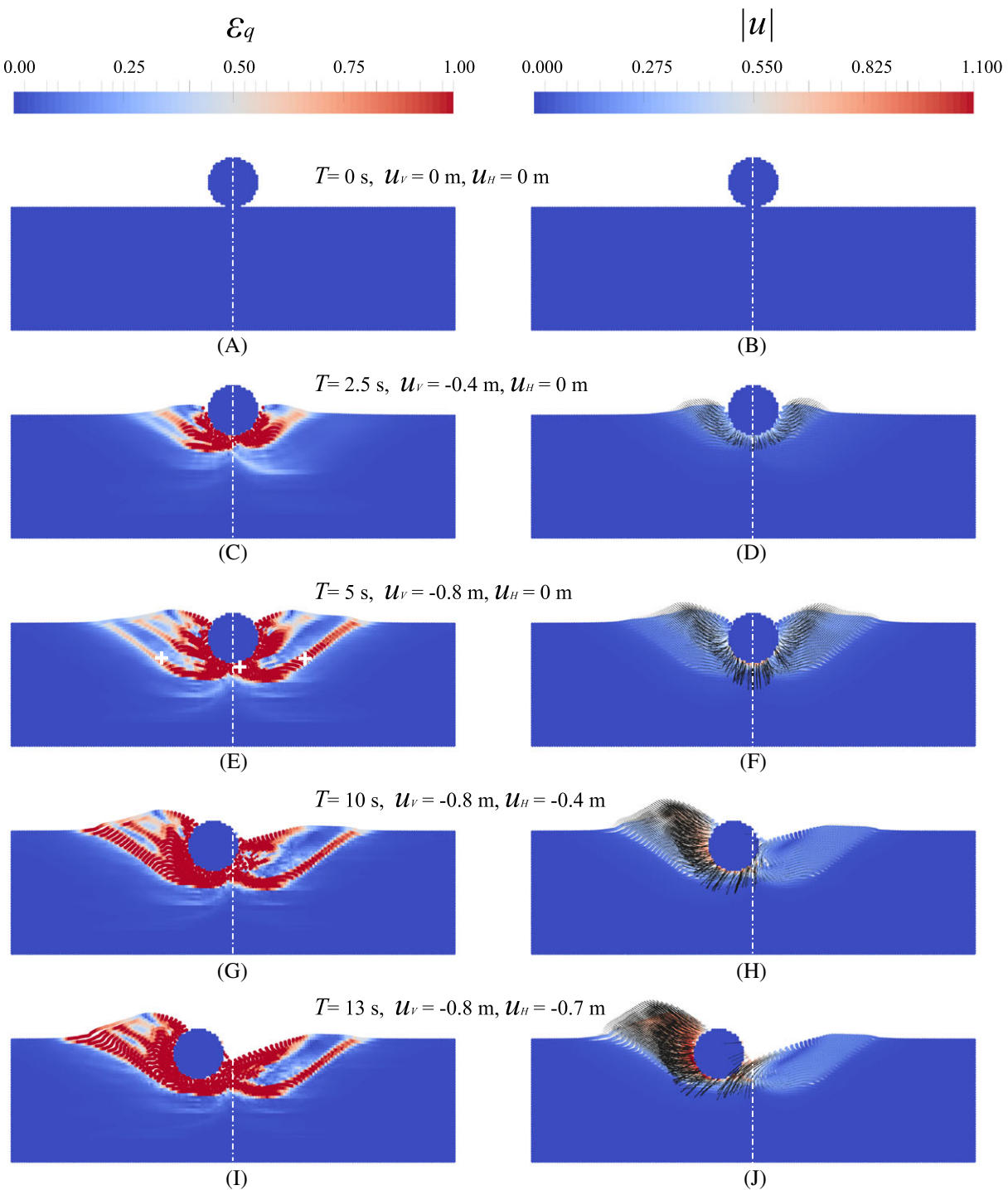


**FIGURE 22** Contour of deviatoric strain  $\epsilon_q$  and displacement field  $\mathbf{u}$  in soil-pipe interaction problem [Colour figure can be viewed at [wileyonlinelibrary.com](http://wileyonlinelibrary.com)]

in Figure 24 indicates the onset of lateral movement of pipe. At this time instance,  $\epsilon_q = 0.5$ ,  $|\theta| = 10^\circ$  for Point D and  $\epsilon_q = 1.2$ ,  $|\theta| = 30^\circ$  for Point F), which is consistent with Figure 22E. The stress responses at both points show a softening stress drop, notwithstanding certain fluctuations.

Different from Points D and F which are largely of shearing characteristics, Point E exhibits typical compression responses (note that the slope of the stress path of penetration state, colored in blue in Figure 24E, is smaller than 1). Note that Point E is not perfectly located at the bottom of the pipe, it is pushed downward with slight deviation to the right (Figure 23). The continuous compression by the pipe pushes up the mean stress  $p$ , up to an order higher magni-

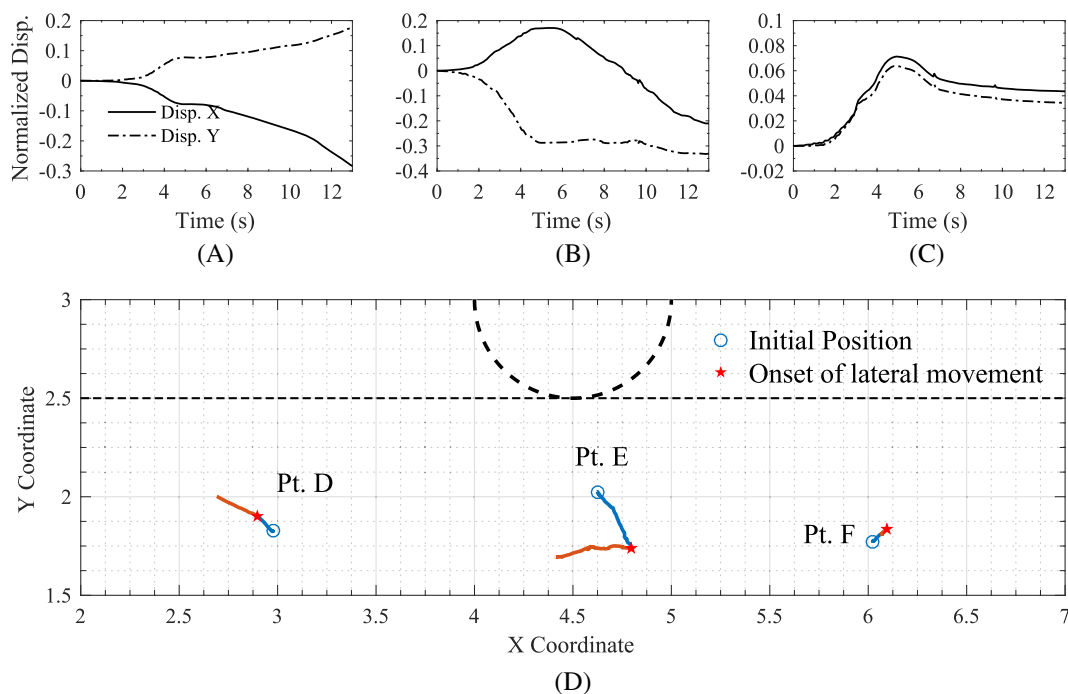


**FIGURE 23** Displacement evolution of Point D, E, and F (A-C) and their trajectory (D) in soil-pipe interaction problem [Colour figure can be viewed at [wileyonlinelibrary.com](http://wileyonlinelibrary.com)]

tude of 700 kPa than that of Point D and F, before dropping. The deviatoric strain  $\epsilon_q$  for Point E rises rapidly to a large value, which can be mainly attributed to the increasing difference between  $\epsilon_{xx}$  and  $\epsilon_{yy}$  induced by compression. The rotation  $\theta$  at Point E remains nearly zero despite some fluctuations, indicating no apparent shearing is pertinent to this point.

### Lateral movement stage

When the pipe begins to displace laterally, Point D and Point F show rather different responses. Since the shear band on the left where Point D is located is enhanced by the lateral movement of the pipe, both deviatoric strain  $\epsilon_q$  and rotation  $\theta$  at Point D increase significantly (from 0.5 to 2.6 for  $\epsilon_q$  and from 15° to 58° for  $\theta$ ). The trajectory of Point D shows a continuous laterally upward trend following the vertical penetration stage (Figure 23). The stress path of Point D in Figure 24B shows strong fluctuations, apparently complicated by the fact of the rough surface of the pipe and the possible change of principal stress directions in the passive zone pushed by the pipe as well as the shear band evolution. In contrast to Point D, the stress responses shown by Point F during the lateral movement of pipe is rather different. Located on the right of the pipe, Point F is in the active zone when the pipe moves left. As the pipe moves to the left, the soil behind the pile close to the middle shear band formed in the penetration stage (see Figure 22G) slips down to fill the gap, but the main shear band at the bottom, in where Point F is located, is not significantly affected. Therefore, the position, the deviatoric strain  $\epsilon_q$ , and rotation  $\theta$  for Point F do not experience marked changes (eg,  $\epsilon_q$  only increases from 1.3 to 1.4). Although its movement and deformation do not show apparent change, Point F does show apparent changes in the stress state. When the soil slides down along the shear bands, the confining pressure at Point F is low and therefore, leading to a reversed stress path heading toward the origin. When the soil becomes steady again, the confining pressure is gradually recovered and thus, both  $p$  and  $q$  rebound back to low but non-zero values ( $p \approx 15$  kPa,  $q \approx 4$  kPa). Unlike in the penetration stage, Point E suffered significant shearing rather than compression during the lateral pipe movement. Its stress path during lateral movement state, which is plotted in red in Figure 24H, shows strong fluctuations and possesses a slope larger than 1. The mean stress  $p$  for Point E generally maintains at a relatively low value throughout the lateral pipe movement because most of soil originally above the Point E is pushed to the left, mobilizing Point E to the left together with an anticlockwise rolling. This processing lead to a continue increase in deviatoric strain  $\epsilon_q$  and rotation  $\theta$ .

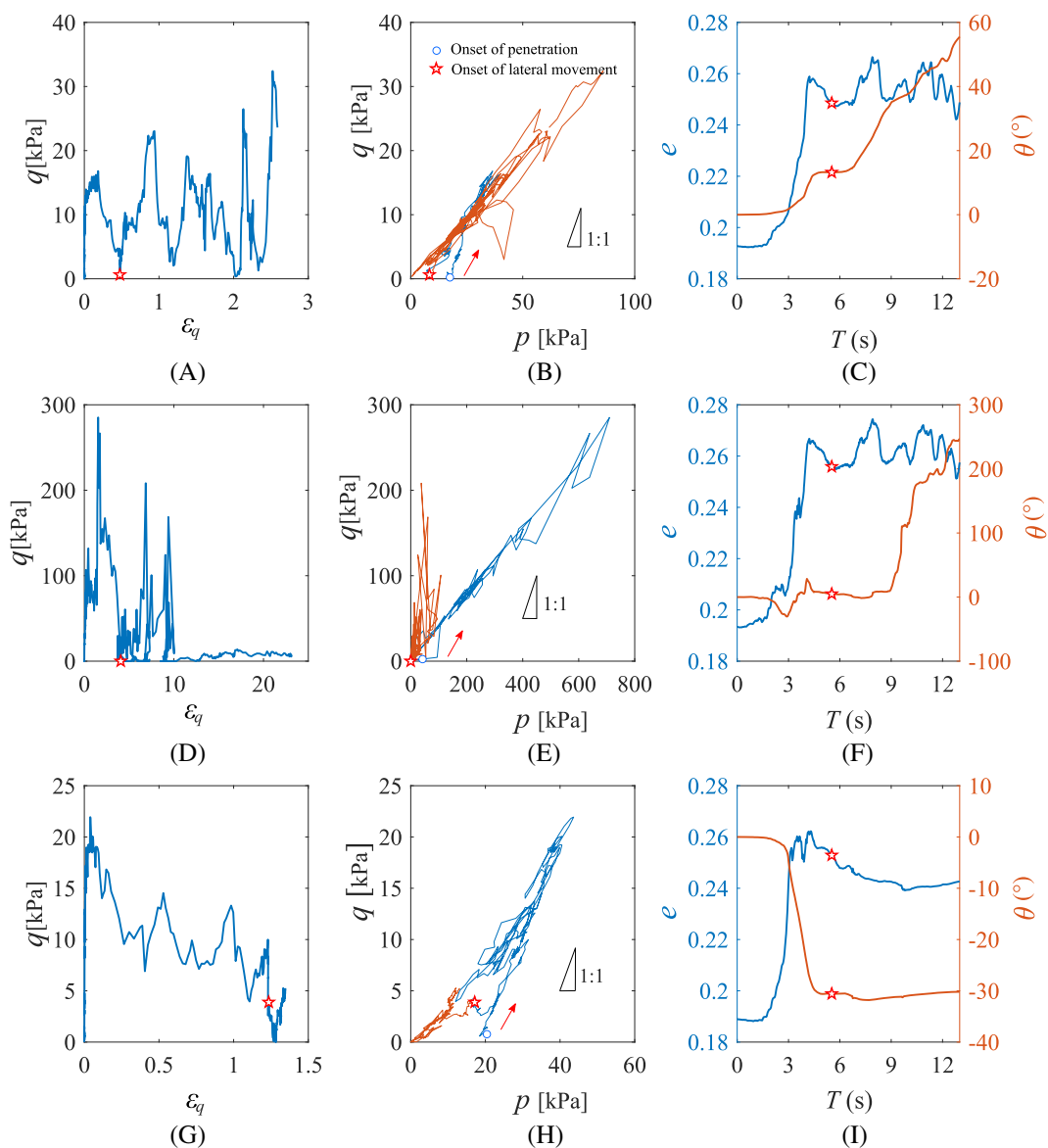


**FIGURE 24** Local response of selected material points in soil-pipe interaction problem. (A-C) Point D, (D-F) Point E, and (G-I) Point F [Colour figure can be viewed at [wileyonlinelibrary.com](http://wileyonlinelibrary.com)]

### 3.5 | Column collapse

The final example chosen for demonstration is coupled MPM/DEM modeling of a dynamic problem. We consider the collapse of a soil column onto level ground, a classical dynamic problem having received extensive experimental investigations.<sup>84-87</sup>

The geometry and the boundary conditions of the soil column are shown in Figure 25. The soil column is 1 m in both width and height. A smooth gate is placed at its right side to control the collapse. The base is also modeled using a rigid material to provide bottom frictions for the soil during collapse. The friction coefficient between the base and the soil adopts a value of 0.4. This value plays a minor role for the entire collapse process since the main body of soil indeed flows over a thin layer adhering to the base.<sup>20,86</sup> A symmetry boundary is assumed for the left side of the soil column. The whole soil column was divided by  $16 \times 16$  elements with four material points per cell (four PPC). The RVEs are prepared using the parameters listed in Table 3. One thousand particles have been used in each RVE. Again, each RVE is isotropically consolidated in the DEM solver to its corresponding geostatic pressure before assigning to the material point in MPM. To speed up the simulation, rolling resistance has not been considered. Meanwhile, a relatively small value of PIC,  $5.0 \times 10^{-4}$ , has been adopted to provide necessary stability without altering the energy conservation.<sup>61</sup>

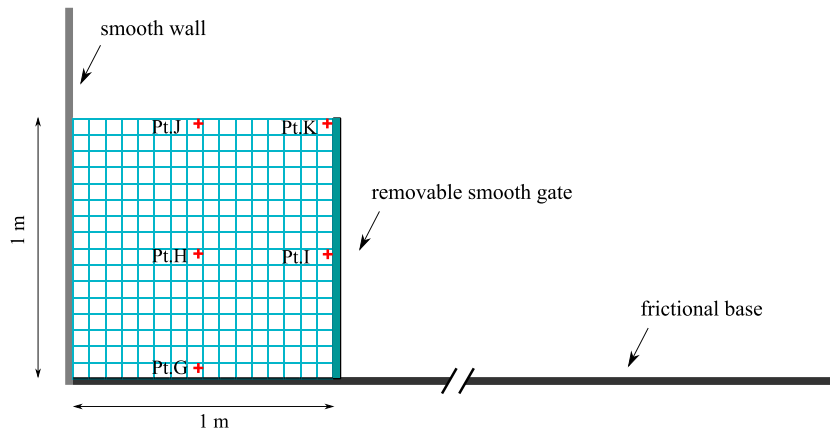


**FIGURE 25** Model setup for the column collapse problem. Selected particles for meso-scale analysis is marked as red cross [Colour figure can be viewed at [wileyonlinelibrary.com](http://wileyonlinelibrary.com)]

**TABLE 3** Discrete element method (DEM) parameters for representative volume elements (RVEs) used in column collapse problem

Particle Num.	$r(\text{mm})$	$\rho(\text{kg}/\text{m}^3)$	$E(\text{MPa})$	$\nu$	$\varphi(\circ)$	$\alpha$	$e_0$
1000	3-7	2650	600	0.8	28.6	0.1	0.197-0.226

### 3.5.1 | Flow patterns

The collapsing process of the soil column is demonstrated in Figure 26. We choose the deviatoric strain  $\epsilon_q$  and the velocity profile  $\mathbf{v}$  to demonstrate the collapse and settling process. The two quantities offer a complementary picture in characterizing the collapsing process,  $\epsilon_q$  describes the cumulative deformation during the collapse, while  $\mathbf{v}$  provides a transient characterization of the kinematic field of the soil. The collapse is initiated instantly with the removal of the smooth gate. Notably, the initial failure occurs at the bottom right corner of the soil column and further propagates vertically towards the top surface and inward to the column along an approximate circular surface (better seen from the velocity profile). The circular interface (shown as a white dash line) marks the boundary between mobilized collapsing zone and the temporal static zone. During  $T = 0.2\text{-}0.7 \text{ s}$ , the collapsing soil touches the frictional base and is gradually slowed down, while the top left portion of the soil column is mobilized to collapse and flow down over a thin stationary layer close to the base. The inset in Figure 26F magnifies the composition of the middle part of the main flow consisting of: (a) an upper steady fast flowing layer, (b) middle layer with a large velocity gradient, and (c) a lower layer lying adjacent to the static zone over which the flow velocity descends gradually to 0. The other inset in Figure 26F shows the significant effect of shearing at the flow front imposed by the stationary soil or based immediate in contact. During  $T = 0.7\text{-}1.3 \text{ s}$ , the frontal part ceases to move at about 3 m from the origin, while the stationary layer in contact with the base continues to build up, resulting in a rising mobilized-static interface. Only a shallow portion of the surface soil located in the middle still remains with certain velocity. This stage is termed as avalanching stage by some researchers.<sup>20,86</sup> At the final stage ( $T = 1.6 \text{ s}$ ), when all soil settles down and become immobilized, the observed deposition profile is consistent with experimental result reported in Lube et al.<sup>86</sup> The perpetual dead zone of the soil column that has never been mobilized throughout the whole collapse process forms a triangular wedge (marked as blue in Figure 26I), with an angle to the ground surface of 39°.

The normalized run out distance can be calculated using:

$$d^* = (d_f - d_0)/d_0, \quad (48)$$

where  $d_f$  is the distance between the farthest point and the origin (after removing the scatter points, which is not in contact with the main deposit) and  $d_0$  is the initial width of the column. In the present study, the normalized runout distance is calculated as  $d^* = 1.8$ , which is slightly larger than the experimental observations of 1.6.<sup>86</sup> This discrepancy may be because of two reasons: (1) The DEM employs cylinder rods to simulate the granular particles, leading to a plane strain approximation. This may underestimate the interparticle frictions out of the plane direction and hence less energy dissipation. (2) In reality, a considerable part of soil fell down with intensive rolling and sliding (resistance) which cause

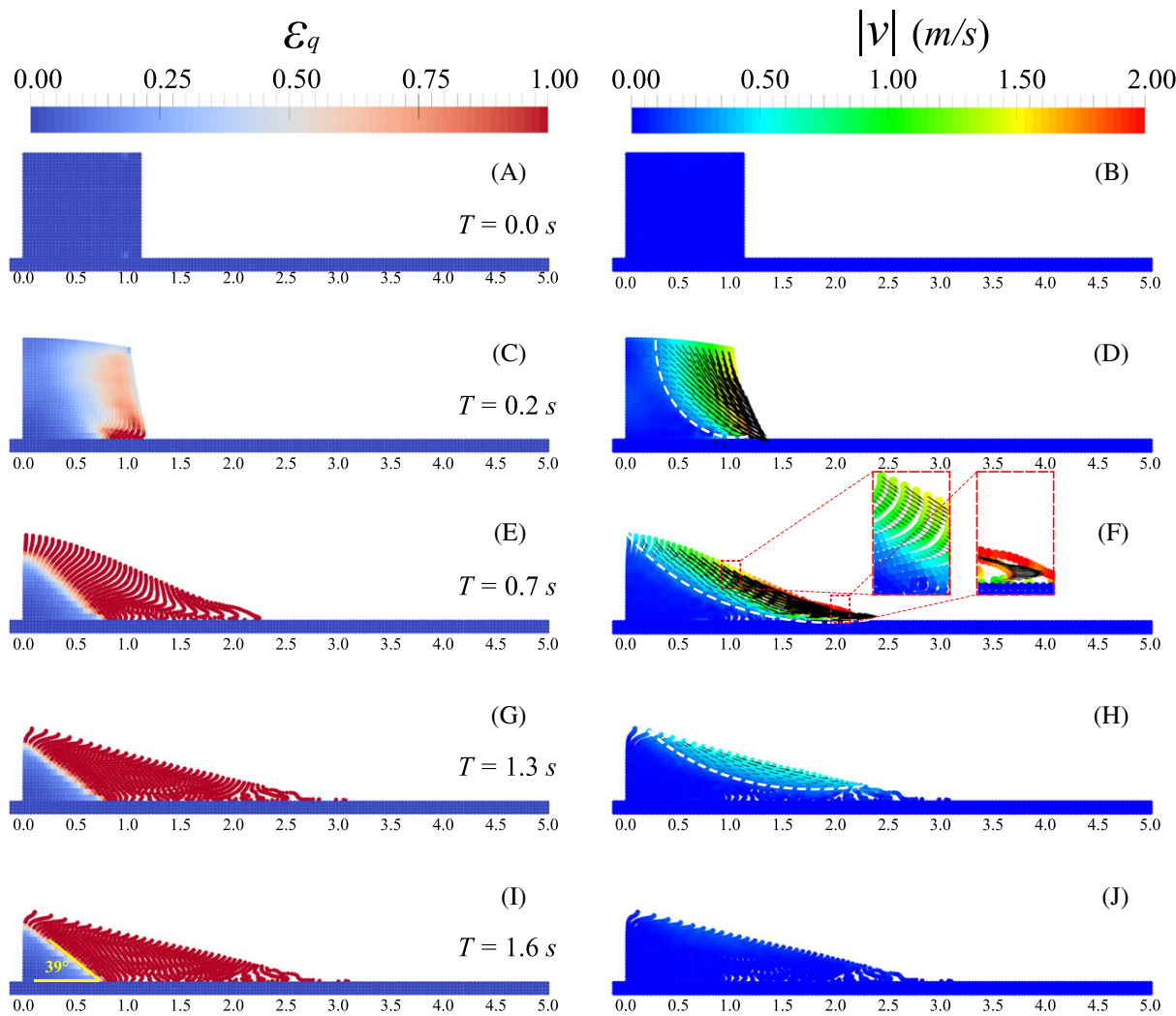


**FIGURE 26** Contour of deviatoric strain  $\epsilon_q$  and velocity field  $v$  in column collapse problem. The white dashed line indicates the interface between current static and mobilizing zone [Colour figure can be viewed at [wileyonlinelibrary.com](http://wileyonlinelibrary.com)]

intensive energy dissipation, while the present study considers free-rolling DEM model (the reader can refer to Kermani et al<sup>63</sup> for the effect of rolling resistance on column collapse).

### 3.5.2 | Energy evolution and local responses

The evolution of energy during the collapse of column is further explored. The energies normalized by the initial potential energy are plotted in Figure 27, where the initial potential energy  $E_p^0$ , the potential energy  $E_p^t$ , the kinematic energy  $E_k^t$ , and the dissipated energy  $E_d^t$  are respectively calculated according to:  $E_p^0 = \sum_p m_p g z_p^0$ ,  $E_p^t = \sum_p m_p g z_p^t$ ,  $E_k^t = \sum_p \frac{1}{2} m_p (v_p^t)^2$ , and  $E_d^t = E_p^0 - E_p^t - E_k^t$ . As can be seen, since the onset of the collapse, the potential energy of the soil column steadily drops, fueling energy that is transformed into kinematic energy and dissipated energy before becoming steady when all soils settle down. The kinematic energy of the soil column increases to reach a peak ( $E_d^t/E_p^0 = 0.1$ ) at around 0.4 s before gradually decreasing to 0. The normalized total energy dissipated during the collapse increases steadily and reaches a final steady value of 0.55, which is smaller than the semi-empirical prediction  $E_d^t/E_p^0 = 1 - 0.74/2a = 0.63$  according to Lajeunesse et al.<sup>84</sup> The attributable reasons to the difference have been discussed in last subsection.

To compare the difference in local material response, several material points are chosen (see Figure 25 for their positions) for monitoring throughout the collapse process. Figure 28 shows the evolution of displacement and the flow path of each monitored point. Apparently, the horizontal and vertical displacements at different locations evolve in a different manner. For horizontal displacement, the two points at the right surface (I & K) evolve faster, followed by Point J on the top surface and Point H in the column center. For vertical displacement, the top right corner Point K evolves the fastest.

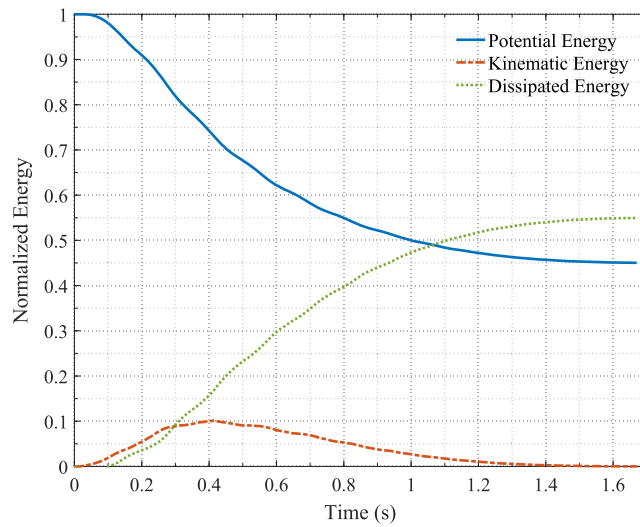


**FIGURE 27** Energy evolution during the column collapse [Colour figure can be viewed at [wileyonlinelibrary.com](http://wileyonlinelibrary.com)]

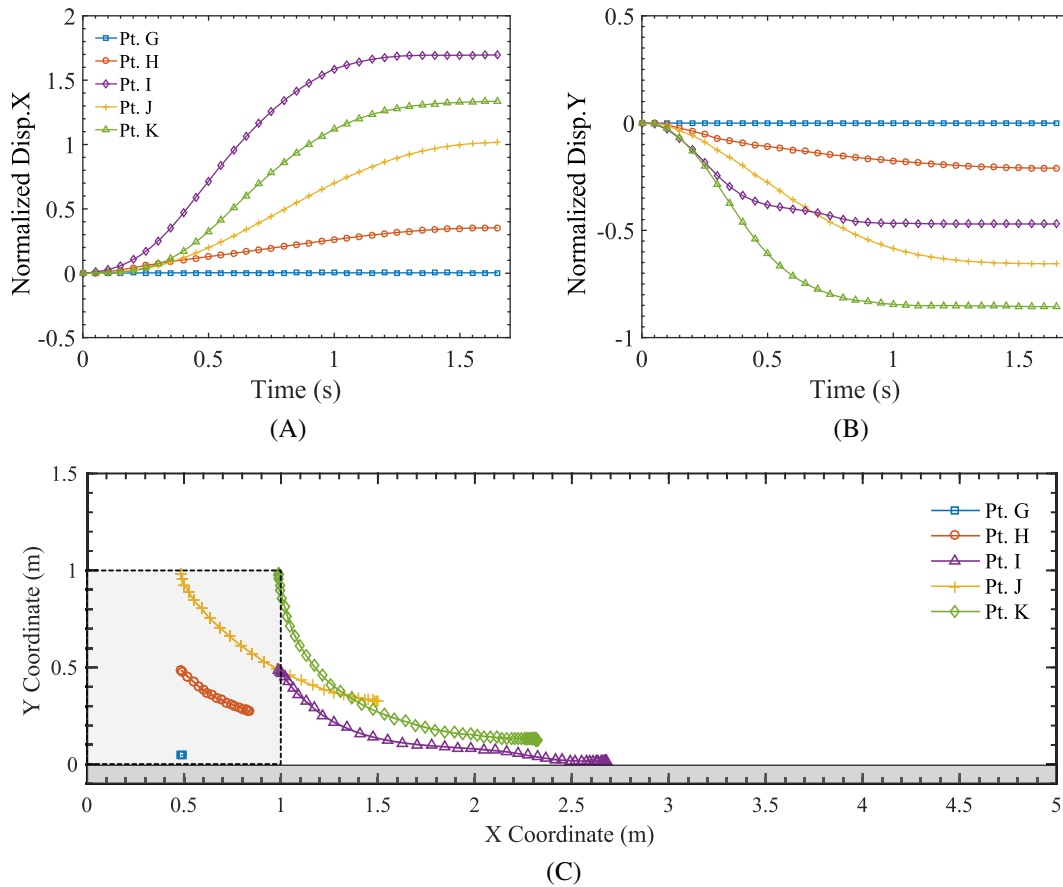


**FIGURE 28** Evolution of displacement A, and B, and flow trajectory C, for the five selected material points during the column collapse [Colour figure can be viewed at [wileyonlinelibrary.com](http://wileyonlinelibrary.com)]

Point I shows an initial faster vertical displacement than Point J, but later, the former is overtaken by Point J at around 0.75 s. The bottom Point G is totally immobilized at all. In terms of flow trajectory, the four upper points (J, K, H, I) travel similarly along a concave path.

## 4 | CONCLUSIONS

A coupled MPM/DEM approach has been presented for multiscale modeling of large deformation problems in geomechanics. A hierarchical coupling scheme is employed to model a boundary value problem by MPM and to derive the necessary constitutive response from the DEM solution for the RVE embedded in each material point of the MPM. The two-way information passing scheme between MPM and DEM enables highly nonlinear, state- and load-dependent material responses of granular materials to be rigorously captured, which is critical for large deformation geomechanics problems, and meanwhile conveniently avoids the necessity of phenomenological constitutive assumptions that are essential in conventional MPM approaches. The multiscale method retains the predictive capability of MPM in tackling large deformation problems and further furnishes advantageous features of direct relating macro observations to underlying microstructural origins and physical mechanisms. The proposed multiscale approach has been validated by a single element test and has further been employed to model four typical geomechanics problems involving large deformation, including biaxial compression, rigid footing, soil-pipe interaction, and soil column collapse. The detailed coupling procedure and some key findings from the numerical examples are summarized as follows:

1. In hierarchical coupling of MPM and DEM, the incremental displacement gradient at each material point in MPM is passed to its corresponding RVE as boundary conditions to solve the RVE using the DEM solver. A Cauchy stress homogenized over the deformed DEM assembly is extracted and transferred back to the MPM for the subsequent computation. In such a sequential coupling scheme, conventional phenomenological constitutive models are no longer needed.
2. Simulation of biaxial compression test and the observation of cross-shape shear bands in the sample demonstrates that the proposed approach is able to faithfully reproduce complex mechanical behavior of granular materials such as strain localization. Examination of the influence of mesh density and PPC number indicates that the MPM/DEM multiscale approach remains mesh-dependent and the influence of mesh density is more apparent than that of the PPC number.
3. The robustness and flexibility of the multiscale modeling approach in dealing with various granular materials are manifested in the simulation of the footing problem. Three RVEs are generated to represent different soils: dense, medium dense, and soft soil. Three typical foundation failure modes are observed, including general shear failure for dense soil, local shear failure for medium dense soil, and punching failure for the soft soil. In the general shear failure, a continuous slip surface is fully developed and extends to the ground surface with an apparent ground heave. This slip surface does not extend to ground surface for the local failure. For punching failure, the influence zone is constrained closely under the footing and no log-spiral slip surface is formed.
4. Modeling of the soil-pipe interaction problem further highlights the true advantages MPM/DEM multiscale approach can offer in dealing with large deformation. In the simulation, the pipe first penetrates into the soil vertically and then moves laterally with a large amplitude of displacement. During the penetration stage, the soil is pushed aside and multiple unsymmetric, interlayered shear bands emerge progressively. When the lateral movement commences, the soil ahead of the pipe is gradually pushed, which intensifies the previously formed shear bands and forms higher heave, while the soil behind the pipe experiences certain stress reversals. Further local analysis of the material response at chosen points confirm the macro observations.
5. The proposed approach has also been applied to modeling of a dynamic problem: the collapse of soil column. The simulated collapsing and flow behaviors are found consistent with experimental observations.<sup>86</sup> Because of ignoring of 3D effect of interparticle frictions and rolling resistance, our multiscale modeling overestimates the runout distance than empirical predictions.

Some modeling details and challenges are noteworthy. Because of excessive large deformation, it is entirely possible in certain extreme cases of multiscale simulations that the attached RVE may deform severely to end up with a rather thin DEM configuration (ie, the depth of packing along the thinnest direction is only 3-4 times of the particle size). Under this circumstance, whether the accuracy of the extracted Cauchy stress is preserved or not needs further study. Since the overall MPM computation follows explicit schemes, care should be taken to choose sufficiently small loading steps to ensure the accuracy of the simulation results. Further studies are needed to find more efficient solutions schemes, ie, adaptive multiscale homogenization,<sup>88</sup> to mitigate the computational cost of the multiscale modeling. It is also desired to enrich the functionalities of current multiscale approach by considering grain morphology,<sup>64,89-91</sup> particle breakage,<sup>39,92</sup> or hydro-mechanical coupling.<sup>26,93</sup> Although all cases discussed in this paper have been based on 2D simulations, it is

straightforward to further implement the code in 3D as the multiscale framework is proposed in generalized form and, both the adopted MPM solver (*NairnMPM*) and DEM solver (*YADE*) have built-in 3D capabilities.

## ACKNOWLEDGEMENTS

The study was financially supported by the National Natural Science Foundation of China (by Project No. 51679207), the Research Grants Council of Hong Kong under the Theme-based Research Scheme (by Project No. T22-603/15-N), and General Research Fund (by Project No. 16210017).

## ORCID

Jidong Zhao  <https://orcid.org/0000-0002-6344-638X>

## REFERENCES

1. Hu Y, Randolph MF. A practical numerical approach for large deformation problems in soil. *Int J Numer Anal Methods Geomech.* 1998;22(5):327-350.
2. Yu L, Liu J, Kong XJ, Hu Y. Three-dimensional RITSS large displacement finite element method for penetration of foundations into soil. *Comput Geotech.* 2008;35(3):372-382.
3. Wang D, Bienen B, Nazem M, et al. Large deformation finite element analyses in geotechnical engineering. *Comput Geotech.* 2015;65:104-114.
4. Borja RI. A finite element model for strain localization analysis of strongly discontinuous fields based on standard Galerkin approximation. *Comput Methods Appl Mech Eng.* 2000;190(11):1529-1549.
5. Borja RI. Finite element simulation of strain localization with large deformation: capturing strong discontinuity using a Petrov-Galerkin multiscale formulation. *Comput Methods Appl Mech Eng.* 2002;191(27-28):2949-2978.
6. Kim J, Armero F. Three-dimensional finite elements with embedded strong discontinuities for the analysis of solids at failure in the finite deformation range. *Comput Methods Appl Mech Eng.* 2017;317:890-926.
7. Armero F, Linder C. New finite elements with embedded strong discontinuities in the finite deformation range. *Comput Methods Appl Mech and Eng.* 2008;197(33-40):3138-3170.
8. Kardani M, Nazem M, Sheng D, Carter JP. Large deformation analysis of geomechanics problems by a combined rh-adaptive finite element method. *Comput Geotech.* 2013;49:90-99.
9. Zhang X, Krabbenhoft K, Pedroso DM, et al. Particle finite element analysis of large deformation and granular flow problems. *Comput Geotech.* 2013;54:133-142.
10. Monaghan JJ. Smoothed particle hydrodynamics. *Rep Prog Phys.* 2005;68(8):1703.
11. Lucy LB. A numerical approach to the testing of the fission hypothesis. *Astron J.* 1977;82:1013-1024.
12. Liu WK, Jun S, Zhang YF. Reproducing Kernel particle methods. *Int J Numer Methods Fluids.* 1995;20(8-9):1081-1106.
13. Nguyen VP, Rabczuk T, Bordas S, Duflot M. Meshless methods: a review and computer implementation aspects. *Math Comput Simul.* 2008;79(3):763-813.
14. Sulsky D, Chen Z, Schreyer HL. A particle method for history-dependent materials. *Comput Meth Appl Mech Eng.* 1994;118(1):179-196.
15. Sulsky D, Zhou SJ, Schreyer HL. Application of a particle-in-cell method to solid mechanics. *Comput Phys Commun.* 1995;87(1-2):236-252.
16. Bardenhagen SG, Kober EM. The generalized interpolation material point method. *Comput Model Eng Sci.* 2004;5(6):477-496.
17. Sołowski WT, Sloan SW. Evaluation of material point method for use in geotechnics. *Int J Numer Anal Methods Geomech.* 2015;39(7):685-701.
18. Phuong NTV, van Tol AF, Elkadi ASK, Rohe A. Numerical investigation of pile installation effects in sand using material point method. *Comput Geotech.* 2016;73:58-71.
19. Lorenzo R, da Cunha RP, Neto MP, Nairn JA. Numerical simulation of installation of jacked piles in sand using material point method. *Can Geotech J.* 2018;55(1):131-146.
20. Fern EJ, Soga K. The role of constitutive models in mpm simulations of granular column collapses. *Acta Geotech.* 2016;11(3):659-678.
21. Mast CM. Modeling landslide-induced flow interactions with structures using the material point method. *PhD thesis.* United States: University of Washington; 2013.
22. Wiećkowski Z. The material point method in large strain engineering problems. *Comput Meth Appl Mech Eng.* 2004;193(39-41):4417-4438.
23. Andersen S, Andersen L. Modelling of landslides with the material-point method. *Comput Geosci.* 2010;14(1):137-147.
24. Llano-Serna MA, Farias MM, Pedroso DM. An assessment of the material point method for modelling large scale run-out processes in landslides. *Landslides.* 2016;13(5):1057-1066.
25. Abe K, Soga K, Bandara S. Material point method for coupled hydromechanical problems. *J Geotech Geoenvir Eng.* 2014;140(3):04013033.
26. Bandara S, Soga K. Coupling of soil deformation and pore fluid flow using material point method. *Comput Geotech.* 2015;63:199-214.
27. Soga K, Alonso E, Yerro A, Kumar K, Bandara S. Trends in large-deformation analysis of landslide mass movements with particular emphasis on the material point method. *Géotechnique.* 2016;66(3):248-273.

28. Liu C, Sun Q, Jin F, Zhou GG. A fully coupled hydro-mechanical material point method for saturated dense granular materials. *Powder Technol.* 2017;314:110-120.
29. Gao Z, Zhao J. Strain localization and fabric evolution in sand. *Int J Solids Struct.* 2013;50(22-23):3634-3648.
30. Gao Z, Zhao J. Constitutive modeling of artificially cemented sand by considering fabric anisotropy. *Comput Geotech.* 2012;41:57-69.
31. Zhao J, Guo N. Rotational resistance and shear-induced anisotropy in granular media. *Acta Mech Solida Sin.* 2014;27(1):1-14.
32. Zhao J, Gao Z. Unified anisotropic elastoplastic model for sand. *J Eng Mech.* 2015;142(1):04015056.
33. Zhao J, Guo N. Unique critical state characteristics in granular media considering fabric anisotropy. *Géotechnique.* 2013;63(8):695.
34. Gao Z, Zhao J, Li XS, Dafalias Yannis F. A critical state sand plasticity model accounting for fabric evolution. *Int J Numer Anal Methods Geomech.* 2014;38(4):370-390.
35. Gao Z, Zhao J. A non-coaxial critical-state model for sand accounting for fabric anisotropy and fabric evolution. *Int J Solids Struct.* 2017;106:200-212.
36. Cundall PA, Strack OD. A discrete numerical model for granular assemblies. *Géotechnique.* 1979;29(1):47-65.
37. Guo N, Zhao J. The signature of shear-induced anisotropy in granular media. *Comput Geotech.* 2013;47:1-15.
38. Wang G, Wei J. Microstructure evolution of granular soils in cyclic mobility and post-liquefaction process. *Granular Matter.* 2016;18(3). Article ID 51.
39. Wang J, Yan H. On the role of particle breakage in the shear failure behavior of granular soils by DEM. *Int J Numer Anal Methods Geomech.* 2013;37(8):832-854.
40. Teufelsbauer H, Wang Y, Pudasaini SP, Borja RI, Wu W. DEM simulation of impact force exerted by granular flow on rigid structures. *Acta Geotech.* 2011;6(3):119-133.
41. Yuan C, Chareyre B, Darve F. Pore-scale simulations of drainage in granular materials: finite size effects and the representative elementary volume. *Adv Water Res.* 2016;95:109-124.
42. Andrade JE, Avila CF, Hall SA, Lenoir N, Viggiani G. Multiscale modeling and characterization of granular matter: from grain kinematics to continuum mechanics. *J Mech Phys Solids.* 2011;59(2):237-250.
43. Guo N, Zhao J. A coupled FEM/DEM approach for hierarchical multiscale modelling of granular media. *Int J Numer Methods Eng.* 2014;99(11):789-818.
44. Nguyen TK, Combe G, Caillerie D, Desrues J. FEM x DEM modelling of cohesive granular materials: numerical homogenisation and multi-scale simulations. *Acta Geophys.* 2014;62(5):1109-1126.
45. Guo N, Zhao J, Sun W. Multiscale analysis of shear failure of thick-walled hollow cylinder in dry sand. *Géotech Lett.* 2016;6(1):77-82.
46. Guo N. Multiscale characterization of the shear behavior of granular media. *PhD thesis.* Hong Kong: Hong Kong University of Science and Technology; 2014.
47. Zhao J, Guo N. The interplay between anisotropy and strain localisation in granular soils: A multiscale insight. *Géotechnique.* 2015;65(8):642-656.
48. Guo N, Zhao J. 3D multiscale modeling of strain localization in granular media. *Comput Geotech.* 2016;80:360-372.
49. Liu Y, Sun W, Yuan Z, Fish J. A nonlocal multiscale discrete-continuum model for predicting mechanical behavior of granular materials. *Int J Numer Methods Eng.* 2016;106(2):129-160.
50. Guo N, Zhao J. Multiscale insights into classical geomechanics problems. *Int J Numer Anal Methods Geomech.* 2016;40(3):367-390.
51. Wu H, Zhao J, Guo N. Multiscale insights into borehole instabilities in high-porosity sandstones. *J Geophys Res: Solid Earth.* 2018;123(5):3450-3473.
52. Liang W, Zhao J. Multiscale modelling of large deformations in granular materials. In: Su ZQ, Cheng L, eds. *Proceedings of The 21st Annual Conference of HKSTAM 2017 in Conjunction with The 13th Jiangsu - Hong Kong Forum on Mechanics and Its Application.* Hong Kong: HKSTAM; 2017:50-50.
53. Zhao J, Liang W. Multiscale modeling of large deformation in geomechanics: a coupled MPM-DEM approach. In: Wu W, Yu HS, eds. *Proceedings of China-Europe Conference on Geotechnical Engineering. Springer Series in Geomechanics and Geoengineering.* Gwerbestrasse, Switzerland: Springer Nature Switzerland AG; 2018:449-452.
54. Liu C, Sun Q, Yang Y. Multi-scale modelling of granular pile collapse by using material point method and discrete element method. *Procedia Eng.* 2017;175:29-35.
55. Brackbill JU, Kothe DB, Ruppel HM. FLIP: A low-dissipation, particle-in-cell method for fluid flow. *Comput Phys Commun.* 1988;48:25-38.
56. Harlow FH. The particle-in-cell computing method for fluid dynamics. *Methods Comput Phys.* 1964;3:319-343.
57. Brackbill JU, Ruppel HM. FLIP: a method for adaptively zoned, particle-in-cell calculations of fluid flows in two dimensions. *J Comput Phys.* 1986;65(2):314-343.
58. Hammerquist CC, Nairn JA. A new method for material point method particle updates that reduces noise and enhances stability. *Comput Meth Appl Mech Eng.* 2017;318:724-738.
59. Nairn JA. Numerical simulation of orthogonal cutting using the material point method. *Eng Fract Mech.* 2015;149:262-275.
60. Stomakhin A, Schroeder C, Chai L, Joseph T, Selle A. A material point method for snow simulation. *ACM Trans Graphics.* 2013;32(4):1.
61. Jiang C, Schroeder C, Teran J. An angular momentum conserving affine-particle-in-cell method. *J Comput Phys.* 2017;338:137-164.
62. Mindlin RD. Elastic spheres in contact under varying oblique forces. *J Appl Mech.* 1953;20:327-344.
63. Kermani E, Qiu T, Li T. Simulation of collapse of granular columns using the discrete element method. *Int J Geomech.* 2015;15(6):04015004.

64. Kawamoto R, Andò E, Viggiani G, Andrade J. All you need is shape: predicting shear banding in sand with LS-DEM. *J Mech Phys Solids*. 2018;111:375-392.
65. Christoffersen J, Mehrabadi MM, Nemat-Nasser S. A micromechanical description of granular material behavior. *J Appl Mech*. 1981;48(2):339.
66. Nicot F, Hadda N, Guessasma M, Fortin J, Millet O. On the definition of the stress tensor in granular media. *Int J Solids Struct*. 2013;50(14-15):2508-2517.
67. Satake M. Fabric tensor in granular materials. In: IUTAM Conference on Deformation and Flow of Granular Materials; 1982; AA Balkema:63-68.
68. Oda M. Fabric tensor for discontinuous geological materials. *Soils Found*. 1982;22(4):96-108.
69. Nairn JA. Material point method (NairnMPM) and finite element analysis (NairnFEA) open-source software. URL <https://github.com/nairnj/nairn-mpmfea>. 2011.
70. Smilauer V, Catalano E, Chareyre B, et al. *Yade Documentation*. 2nd ed. Grenoble, France: Zenodo; 2015.
71. Bardenhagen SG. Energy conservation error in the material point method for solid mechanics. *J Comput Phys*. 2002;180(1):383-403.
72. Guo N, Zhao J. Parallel hierarchical multiscale modelling of hydro-mechanical problems for saturated granular soils. *Comput Meth Appl Mech Eng*. 2016;305:31-67.
73. Askes H, Rodríguez-Ferran A. A combined rh-adaptive scheme based on domain subdivision. Formulation and linear examples. *Int J Numer Methods Eng*. 2001;51(3):253-273.
74. Linder C, Armero F. Finite elements with embedded strong discontinuities for the modeling of failure in solids. *Int J Numer Methods Eng*. 2007;72(12):1391-1433.
75. Steffen M, Kirby RM, Berzins M. Analysis and reduction of quadrature errors in the material point method (MPM). *Int J Numer Methods Eng*. 2008;76(6):922-948.
76. Desrues J, Argilaga A, Dal PS, Combe G, Caillerie D, kein Nguyen T. Restoring mesh independency in FEM-DEM multi-scale of strain localization using second gradient regularization. In: Papamichos E, Papanastasiou P, Pasternak E, & Dyskin A Eds. *Bifurcation and Degradation of Geomaterials with Engineering Application. Springer Series in Geomechanics and Geoengineering*. Springer Nature, Switzerland; 2017:53-457.
77. Qiu G, Henke S, Grabe J. Application of a coupled Eulerian–Lagrangian approach on geomechanical problems involving large deformations. *Comput Geotech*. 2011;38(1):30-39.
78. Nazem M, Sheng D, Carter JP, Sloan SW. Arbitrary Lagrangian–Eulerian method for large-strain consolidation problems. *Int J Numer Anal Methods Geomech*. 2008;32(9):1023-1050.
79. Terzaghi K. *Theoretical Soil Mechanics*. London: Chapman And Hall, Limited; 1951.
80. De Beer EE, Vesic A. Etude experimentale de la capacite portante du sable sous des fondations directes etablies en surface. *Ann Trav Publics Belg*. 1958;59(3):5-88.
81. Prandtl L. Hauptaufsätze: Über die eindringungsfestigkeit (Härte) plastischer baustoffe und die festigkeit von schneiden. *ZAMM-J Appl Math Mech/Z Angew Math Mech*. 1921;1(1):15-20.
82. Vesić AS. Analysis of ultimate loads of shallow foundations. *J Soil Mech Found Div*. 1973;99(1):45-73.
83. White DJ, Randolph MF. Seabed characterisation and models for pipeline-soil interaction. *Int J Offshore Polar Eng*. 2007;17(03):193-204.
84. Lajeunesse E, Mangeney-Castelnau A, Villette JP. Spreading of a granular mass on a horizontal plane. *Phys Fluids*. 2004;16(7):2371-2381.
85. Lajeunesse E, Monnier JB, Homsy GM. Granular slumping on a horizontal surface. *Phys fluids*. 2005;17(10):103302.
86. Lube G, Huppert HE, Sparks RSJ, Freundt A. Collapses of two-dimensional granular columns. *Phys Rev E*. 2005;72(4):041301.
87. Lube G, Huppert HE, Sparks RSJ, Hallworth MA. Axisymmetric collapses of granular columns. *J Fluid Mech*. 2004;508:175-199.
88. Rezakhani R, Zhou X, Cusatis G. Adaptive multiscale homogenization of the lattice discrete particle model for the analysis of damage and fracture in concrete. *Int J Solids Struct*. 2017;125:50-67.
89. Mollon G, Zhao J. Characterization of fluctuations in granular hopper flow. *Granular Matter*. 2013;15(6):827-840.
90. Mollon G, Zhao J. 3D generation of realistic granular samples based on random fields theory and fourier shape descriptors. *Comput Meth Appl Mech Eng*. 2014;279:46-65.
91. Kawamoto R, Andò E, Viggiani G, Andrade JE. Level set discrete element method for three-dimensional computations with triaxial case study. *J Mech Phys Solids*. 2016;91:1-13.
92. Zhu F, Zhao J. A peridynamic investigation on crushing of sand particles. *Géotechnique*. 2018. in press <https://doi.org/10.1680/jgeot.17.p.274>
93. Tampubolon AP, Gast Te, Klár G, et al. Multi-species simulation of porous sand and water mixtures. *ACM Trans Graphics*. 2017;36(4):1-11.

**How to cite this article:** Liang W, Zhao J. Multiscale modeling of large deformation in geomechanics. *Int J Numer Anal Methods Geomech*. 2019;43:1080–1114. <https://doi.org/10.1002/nag.2921>